Role of infarct scar dimensions, border zone repolarization properties and anisotropy in the origin and maintenance of cardiac reentry

P. Colli Franzone [*]   V. Gionti [†]   L. F. Pavarino[*]   S. Scacchi [‡]   C. Storti[†].

September 18, 2019

Abstract

Cardiac ventricular tachycardia (VT) is a life-threatening arrhythmia consisting of a well organized structure of reentrant electrical excitation pathways. Understanding the generation and maintenance of the reentrant mechanisms, which lead to the onset of VT induced by premature beats in presence of infarct scar, is one of the most important issues in current electrocardiology. We investigate, by means of numerical simulations, the role of infarct scar dimension, repolarization properties and anisotropic fiber structure of scar tissue border zone (BZ) in the genesis of VT. The simulations are based on the Bidomain model, a reaction-diffusion system of Partial Differential Equations, discretized by finite elements in space and implicit-explicit finite differences in time. The computational domain adopted is an idealized left ventricle affected by an infarct scar extending transmurally. We consider two different scenarios: i) the scar region extends along the entire transmural wall thickness, from endocardium to epicardium, with the exception of a BZ region shaped as a central sub-epicardial channel (CBZ); ii) the scar region extends transmurally along the ventricular wall, from endocardium to a sub-epicardial surface, and is surrounded by a BZ region (EBZ). In CBZ simulations, the results have shown that: i) the scar extent is a crucial element for the genesis of reentry; ii) the repolarization properties of the CBZ, in particular the reduction of IKs and IKr currents, play an important role in the genesis of reentrant VT. In EBZ simulations, since the possible reentrant pathway is not assigned a-priori, we investigate in depth where the entry and exit sites of the cycle of reentry are located and how the functional channel of reentry develops. The results have shown that: i) the interplay between the epicardial anisotropic fiber structure and the EBZ shape strongly affects the propensity that an endocardial premature stimulus generates a cycle of reentry; ii) reentrant pathways always develop along the epicardial fiber direction; iii) very thin EBZs rather than thick EBZs facilitate the onset of cycles of reentry; iv) the sustainability of cycles of reentry depends on the endocardial stimulation site and on the interplay between the epicardial breakthrough site, local fiber direction and BZ rim.

Keywords: cardiac reentry; Bidomain simulations; infarct border zone; ventricular tachycardia; myocardial infarction

---

[*]Dipartimento di Matematica, Università di Pavia, Via Ferrata 1, 27100 Pavia, Italy. E-mail: colli@imati.cnr.it, luca.pavarino@unipv.it. This work was partially supported by grants of CINECA and of the Istituto di Matematica Applicata e Tecnologie Informatiche, Pavia, Italy

[†]Istituto di cura Città di Pavia, via Parco Vecchio 27, 27100 Pavia, Italy. E-mail: giontiv.md@gmail.com, cesare.storti@gmail.com.

[‡]Dipartimento di Matematica, Università di Milano, Via Saldini 50, 20133 Milano, Italy. E-mail: simone.scacchi@unimi.it. This work was partially supported by grants of Progetto G.N.C.S. of the Istituto Nazionale di Alta Matematica, Roma, Italy

1 Introduction

Sudden cardiac death (SCD) remains one of the most significant causes of death in industrialized countries. The majority of SCDs is due to ventricular arrhythmias, rhythm disorders usually associated with structural heart disease as in patients with myocardial scar due to prior myocardial infarction [45].

In recent studies, myocardial scar extent has emerged as a determinant of the arrhythmic risk in both ischemic (ICM) and non-ischemic cardiomyopathy (NICM) [67, 42, 73, 12]. However, it is interesting to note that clinical characteristics including infarct size and scar extent do not allow to distinguish patients who develop VT early from those who develop it afterwards. On the other hand, there are several studies concerning the electrical and neural remodeling [51, 69], which could lead to refractoriness and conduction abnormalities (see in particular the study [29] for conduction alterations related to post infarction remodeling) contributing to arrhythmogenicity and to high variability of time to first ventricular arrhythmias. In ICM a well-established concept is that the *transition* regions of slow conduction in the surviving myocardium of the infarct border zone (BZ), occurring in post myocardial infarction, have been strongly correlated with increased risk of reentrant ventricular arrhythmias.

The BZ tissue, surrounding an infarct scar, constitutes viable myocardium displaying remodeling with significant different electrophysiological properties with respect to the neighbouring healthy myocardium, i.e. down-regulation of membrane ion channels and transport processes [59, 56]. Previous studies [54, 66, 70] have also shown that in BZ tissue two different remodeling phenomena take place: one associated with the active remodeling related to ion channels across the cell membrane and the other associated with the passive remodeling resulting from the structural tissue changes, such as re-organization of gap junctions distribution, proliferation of fibrotic growth and development of the infarct scar. Moreover, experimental findings have shown that fibrosis can be also induced by reduced sodium channel and connexin expression, yielding a reduction of electrical cell-to-cell coupling responsible for slow electrical activation, see the survey paper [37].

The electrophysiological and structural features underlying a greater risk of onset of VT in patients with myocardial infarction scar are still poorly understood and debated. Computational models of different scar regions can assist in the development of improved methodologies to identify and differentiate arrhythmogenic scar from nonarrhythmogenic scar and also to validate new diagnostic and therapeutic tools in the preclinical setting. Indeed in recent years several modeling and computational studies have tried to fill this gap [20, 21, 22, 14, 15, 16, 19, 81, 5, 10, 76, 33, 36, 40]. In particular, previous Monodomain simulation studies [2, 3, 27] have explored the induction of reentrant arrhythmias in presence of infarct scars surrounded by homogeneous and heterogeneous BZ tissue.

The aim of this study is to investigate by means of Bidomain numerical simulations the role of scar dimension, repolarization and geometric anisotropic properties of the BZ in the genesis and maintenance of reentrant dynamics mimicking a monomorphic ventricular tachycardia. To this end, we consider two different scenarios:

i) the scar region extends along the entire transmural wall thickness, from endocardium to epicardium, with the exception of a BZ shaped as a central sub-epicardial channel, constituting a transition region of viable myocardium;

ii) the scar region extends transmurally along the ventricular wall, from endocardium until a sub-epicardial surface, and it is surrounded by a BZ region of viable myocytes.

We remark that, in the first scenario, the epicardial BZ wedges between two unexcitable regions,

while, in the second scenario, the entire epicardial surface is excitable and the shape of a possible reentrant cycle is not assigned a-priori.

The simulation results have shown that epicardial reentrant pathways can develop inside an EBZ with homogeneous bioeletric properties, following endocardial stimulations. Another important and novel result of the EBZ simulations concerns the role played by the anisotropic structure of the sub-epicardial fibers and the position of the endocardial stimulation site on the induction of reentrant cycles.

2 Methods

2.1 Mathematical models

To model the electrical current flow through the myocardium, we assume the Bidomain representation of the cardiac tissue [77, 44, 26]. The computational electrophysiological model considers three different types of cardiac tissue regions: healthy myocardium, necrotic scar and an infarct border zone (BZ).

Let H denote a three-dimensional portion of myocardium, subdivided into an infarct scar S and a region $\Omega = \Omega_b \cup \Omega_h$ constituted by the BZ Ω_b and the healthy tissue Ω_h, thus $H = \Omega \cup S$. We remark that the scar region S is unexcitable, thus the intracellular space in the normal myocardium Ω is modeled as insulated from S, whereas S as extracellular space can be considered a conducting region in contact with Ω. Moreover, we assume S to be an extracellular isotropic conducting medium.

Therefore, considering as usual in the macroscopic Bidomain modeling the intracellular and extracellular spaces as a superimposed continuous anisotropic ohmic conducting medium connected by a distributed cellular membrane, assuming quasi-static regime, from the current conservation law we obtain:

$$\begin{cases} \operatorname{div} \mathbf{j}_i = -i_m & in \quad \Omega, \quad \mathbf{n}^T \mathbf{j}_i = 0 \quad on \quad \partial\Omega, \\ \operatorname{div} \mathbf{j}_e = i_m & in \quad \Omega, \quad \mathbf{n}^T \mathbf{j}_e = \mathbf{n}^T \mathbf{j}_s \quad on \quad \partial\Omega \cap \partial S \\ \operatorname{div} \mathbf{j}_s = 0 & in \quad S, \quad \mathbf{n}^T \mathbf{j}_s = 0 \quad on \quad \partial S \setminus \partial\Omega, \end{cases} \qquad (1)$$

with $\mathbf{j}_{i,e} = -D_{i,e} \nabla u_{i,e}$ and $\mathbf{j}_o = -\sigma_s \nabla u_s$, (u_i, u_e) the intra- and extracellular potentials in the excitable myocardium tissue and u_s the potential in the scar volume. The source term i_m represents the total transmembrane current per unit volume of the tissue given by the membrane cellular model:

$$i_m = c_m \partial_t v + i_{ion}(v, \mathbf{w}, \mathbf{c}),$$

with $v(\mathbf{x}, t) = u_i(\mathbf{x}, t) - u_e(\mathbf{x}, t)$ the transmembrane potential, $\mathbf{w}$ the gating variables and $\mathbf{c}$ the intracellular ionic concentrations. Moreover, $c_m = \chi C_m$ and $i_{ion} = \chi I_{ion}$, where χ is the area of the cellular membrane surface contained in the unit tissue volume, while C_m, I_{ion} are the membrane capacitance and ion membrane current per unit area of the membrane surface.

The previous system (1) can be rewritten in equivalent form in terms of the transmembrane potential and of the extracellular and scar potentials. Hence, the evolution of the transmembrane potential $v(\mathbf{x}, t)$, extracellular potential u_e, scar potential u_s, gating variables $\mathbf{w}(\mathbf{x}, t)$ and ionic

concentrations $\mathbf{c}(\mathbf{x}, t)$ is described by the macroscopic Bidomain model:

$$
\begin{cases}
c_m \partial_t v - \mathrm{div}(D_i \nabla v) - \mathrm{div}(D_i \nabla u_e) + i_{ion}(v, \mathbf{w}, \mathbf{c}) = i_{app} & \text{in } \Omega \\
\partial_t w - R_w(v, \mathbf{w}, \mathbf{c}) = 0, \quad \partial_t c - R_c(v, \mathbf{w}, \mathbf{c}) = 0 & \text{in } \Omega \\
-\mathrm{div}(D_i + D_e)\nabla u_e = \mathrm{div}\, D_i \nabla v & \text{in } \Omega \\
\mathbf{n}^T D_i \nabla(v + u_e) = 0 & \text{on } \partial\Omega \\
\mathbf{n}^T D_e \nabla u_e = 0 & \text{on } \partial\Omega \setminus \partial S \\
-\mathrm{div}\, \sigma_s \nabla u_s = 0 & \text{in } S \\
u_e = u_s & \text{on } \partial S \cap \partial\Omega \\
\mathbf{n}^T D_e \nabla u_e = \mathbf{n}^T \sigma_s \nabla u_s & \text{on } \partial S \cap \partial\Omega \\
\mathbf{n}^T \sigma_s \nabla u_s = 0 & \text{on } \partial S \setminus \partial\Omega
\end{cases}
\tag{2}
$$

with appropriate initial conditions on $v(\mathbf{x}, 0), \mathbf{w}(\mathbf{x}, 0)$ and $\mathbf{c}(\mathbf{x}, 0)$. Here c_m and i_{ion} denote the capacitance and the ionic current of the membrane per unit volume, i_{app} represents the applied current per unit volume, $D_{i,e}$ are the intra- and extracellular transversely isotropic conductivity tensors and σ_s is the scar conductivity.

We recall that the extracellular potential u_e is defined up to an independent constant $R(t)$ determined by the choice of the reference potential. In this paper, we consider as a reference potential the average of the extracellular/scar potential over the cardiac volume, i.e. we impose $\int_\Omega u_e(\mathbf{x}, t)dx + \int_S u_s(\mathbf{x}, t)dx = 0$.

Assuming transversely isotropic properties of the intra- and extracellular media, the conductivity tensors are given by

$$
D_{i,e} = \sigma_t^{i,e}\, I + (\sigma_l^{i,e} - \sigma_t^{i,e})\mathbf{a}_l \otimes \mathbf{a}_l,
\tag{3}
$$

where $\sigma_l^{i,e}$, $\sigma_t^{i,e}$ are the conductivity coefficients of the intra- and extracellular media measured along the fiber direction $\mathbf{a}_l$ and any cross fiber direction, respectively.

The ionic current is given by $i_{ion} = \chi I_{ion}$, where χ is the membrane surface to volume ratio and the ionic current per unit area of the membrane surface I_{ion} is given by the ten Tusscher membrane model (TP06) [74, 75], available from the cellML depository (models.cellml.org/cellml). The TP06 ionic model also specifies the functions $R_w(v, \mathbf{w})$ and $R_c(v, \mathbf{w}, \mathbf{c})$ in the ordinary differential equations (ODEs) system, consisting of 17 ODEs modeling the main ionic currents dynamics.

2.2 Numerical methods

The space discretization of system (2) is performed by employing hexahedral isoparametric Q_1 finite elements, while the time discretization is based on the following double operator splitting procedure: a) split the ODEs from the PDEs and b) split the elliptic PDE from the parabolic one; for further details see reference [25]. We refer to [80, 82, 57] for other numerical strategies adopted in the literature. This operator splitting strategy yields two large linear systems of algebraic equations that must be solved at each time step. In order to ensure parallelization and portability of our Fortran code, we use the PETSc parallel library [8], a suite of data structures and functions for building large-scale parallel scientific applications, based on the MPI communication library. The parallel strategy employed assigns each subdomain to one processor and the information associated

with the interior of the subdomain is uniquely owned by that processor. The processor stores all subvectors and a block of the matrices (mass, stiffness) associated to each overlapping subdomain. Our parallel code employs different DA (Distributed Arrays) PETSc objects for representing v on the non-scar domain Ω (tissue) and for u_e, u_b on the entire cardiac domain H (non-scar and scar tissue). The two large linear systems at each time step are solved by a parallel conjugate gradient method, preconditioned by the Multilevel Additive Schwarz preconditioner, developed in [58], for the ill-conditioned elliptic system and the Block Jacobi preconditioner for the well conditioned parabolic system. These preconditioners are based on the multilevel PETSc objects PCMG (MultiGrid) with ILU(0) local solvers. The simulations are run on 24 processors of a Linux Cluster with 56 Opteron AMD processors and Infiniband network.

2.3 Simulations setup

2.3.1 Scar with channel border zone (CBZ)

Computational domain. The domain H is the image of a Cartesian periodic slab using ellipsoidal coordinates, yielding a truncated ellipsoid modeling a left ventricle (LV) geometry, described by the parametric equations

$$
\begin{cases}
x = a(r)\cos\theta\cos\phi & \phi_{min} \leq \phi \leq \phi_{max}, \\
y = b(r)\cos\theta\sin\phi & \theta_{min} \leq \theta \leq \theta_{max}, \\
z = c(r)\sin\theta & 0 \leq r \leq 1,
\end{cases}
$$

where $a(r) = a_1 + r(a_2 - a_1)$, $b(r) = b_1 + r(b_2 - b_1)$, $c(r) = c_1 + r(c_2 - c_1)$, and $a_1 = b_1 = 1.5$, $a_2 = b_2 = 2.7$, $c_1 = 4.4$, $c_2 = 5$ (all in cm) and $\phi_{min} = -\pi/2$, $\phi_{max} = 3\pi/2, \theta_{min} = -3\pi/8$, $\theta_{max} = \pi/8$. We will refer to the inner surface of the truncated ellipsoid ($r = 0$) as endocardium and to the outer surface ($r = 1$) as epicardium. In all computations, a structured grid of $512 \times 256 \times 48$ hexahedral isoparametric Q_1 finite elements of size $h \approx 0.02$ cm is used in space, for a total amount of $6\,447\,616$ mesh nodes. Fibers rotate transmurally, linearly with the depth and counterclockwise from epicardium to endocardium, for a total amount of 120°. Two sizes of scar are taken into account: one of dimension about $2 \times 3.5 \times 1$ cm^3 (large scar, see Fig. 1, top panels) and one of dimension $1 \times 1.2 \times 1$ cm^3 (small scar, see Fig. 1, bottom panels). In both cases, the scar extends along the entire transmural thickness, from endocardium to epicardium. In the large scar case, the CBZ consists of the sub-epicardial channel located at the center of the scar (see Fig. 1, top panels) of dimension $0.5 \times 3.4 \times 0.5$ cm^3, whereas in the small scar case, the CBZ consists of the sub-epicardial channel located at the center of the scar (see Fig. 1, bottom panels) of dimension $0.5 \times 1.2 \times 0.5$ cm^3.

Parameter calibration. The values of the transversely isotropic conductivity coefficients in (3), that we use for the healthy tisse in all the numerical tests, are $\sigma_l^i = 3$, $\sigma_t^i = 0.31525$, $\sigma_l^e = 2$, $\sigma_t^e = 1.3514$, all expressed in $m\Omega^{-1}cm^{-1}$; see [23, 24] for the derivation of these conservative values. These values, coupled with the TP06 membrane model, predict conduction velocities of about 0.061 and 0.027 cm/ms for excitation wavefronts propagating along and across the fiber direction, respectively. We remark that these conduction velocities are within the physiological range, see [61, 63]. The membrane surface to volume ratio is $\chi = 10^3$ cm^{-1} and the membrane capacitance per unit volume is $c_m = \chi C_m$, where $C_m = 1$ $\mu F/cm^2$ is the membrane capacitance per unit area. To the scar conductivity σ_s the value of $0.5\,m\Omega^{-1}cm^{-1}$ is assigned. To our knowledge, previous works have considered values of scar conductivity ranging between 0.05 and 0.5 $m\Omega^{-1}cm^{-1}$. We have chosen the value of 0.5 because it is the value closest to the average of the conductivities assigned in the BZ; see below.

Epicardial view   Transmural view

H   BZ   SCAR   H   BZ   SCAR

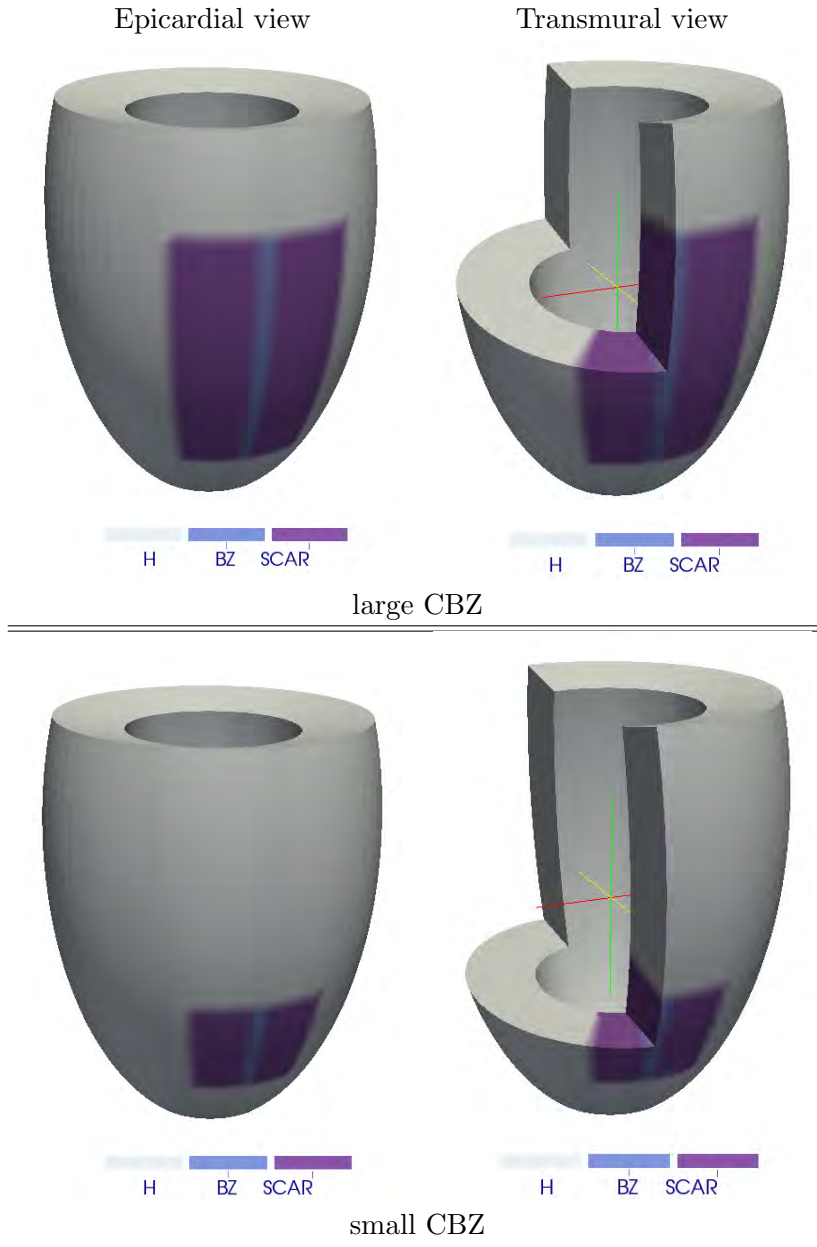large CBZ

H   BZ   SCAR   H   BZ   SCAR

small CBZ

Figure 1: CBZ geometric setup. Epicardial view (left column) and transmural sections (right column) of the idealized left ventricle computational domain with healthy tissue (H, gray), large and small scars (SCAR, purple) and border zones (BZ, blue).

Epicardial view   Transmural views

Thick EBZ   Thin EBZ

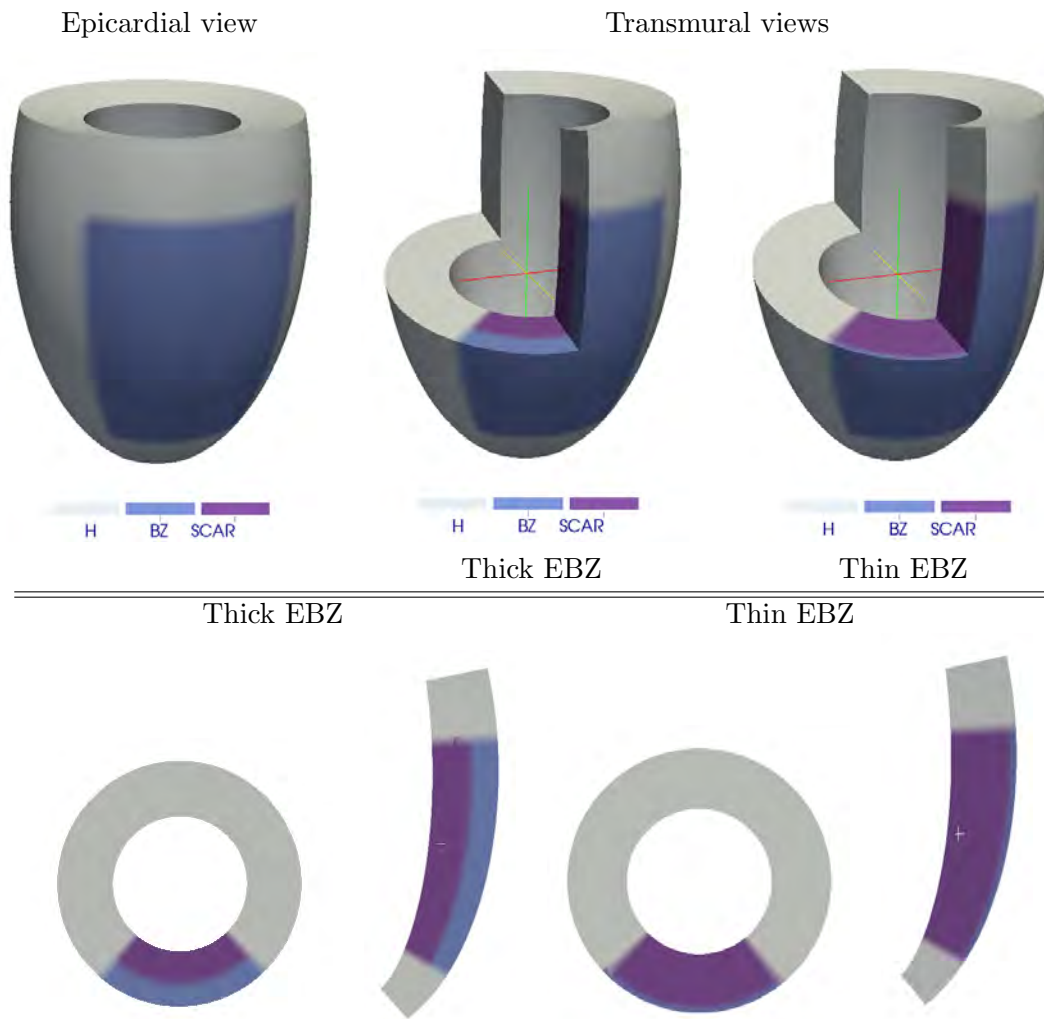Thick EBZ   Thin EBZ

Figure 2: EBZ geometric setup. First row: Epicardial view (left) and transmural sections (center and right) of idealized left ventricle computational domains with healthy tissue (H, gray), scars (SCAR, purple) and thick (center) and thin (right) subepicardial BZ (EBZ, blue). Second and third row: Circumferential (top) and vertical (bottom) sections of thick (left) and thin (right) EBZ.
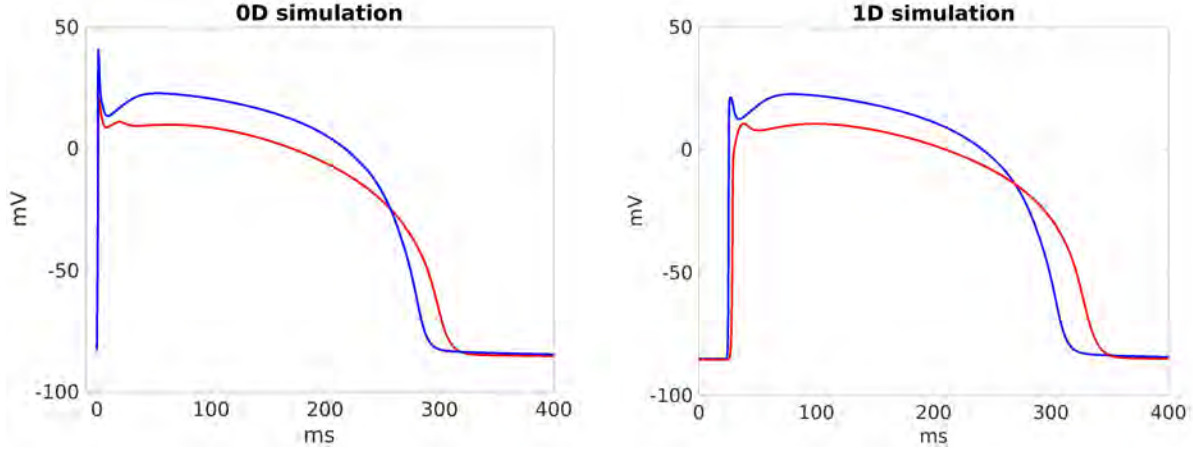
Figure 3: Normal (blue) and border zone (red) action potentials computed from 0D (left) and 1D (right) simulations.

Structural and functional remodeling in healed infarct generates a layer of viable myocardium cells, the so called border zone (BZ) [59, 56]. Actually, the BZ is an heterogeneous region with scar patches [37, 54]. Usually, in canine experiments BZ appears on the epicardium, whereas in human heart it appears on the endocardium. To investigate the morphology and pathways of the infarct-related cycles of reentry, from the macroscopic (averaged) point of view, we approximate the BZ as a homogeneously remodeled region, without changes in fiber direction.

In all simulations, we model the BZ by implementing a 60% reduction of fast sodium current conductance g_{Na} [52, 60, 7, 35], a 70% reduction of L-type calcium current conductance g_{CaL} [59, 39, 7] and a reduction of 70% and 80% of the potassium currents conductances g_{Kr} and g_{Ks}, respectively, [50].

Moreover, the BZ remodeling yields a downregulation and lateralization of connexin 43 [87]. Hence, a loss of the average number of transverse gap-junctions between viable fibers occurs. We model this loss as a 75% reduction of cross fiber intracellular conductivity coefficient σ_t^i. The main characteristics of normal and BZ action potentials for a BCL of 500 msec and a stimulus of 50 $mA\,cm^2$, computed from 0D and 1D simulation on a cardiac fiber of length 3 cm with a central BZ region of 1 cm and using a conductivity of 2 $m\Omega^{-1}cm^{-1}$, are summarized in Table 1, see also Fig. 3. We can see that the BZ AP is characterized by longer duration, decreased upstroke velocity and decreased peak amplitude compared to that of the normal myocardium.

We have compared the dependence of reentry dynamics on the cardiac geometry, on the potassium currents conductances and on the scar dimension by considering the following three settings:

- Channel border zone: left ventricular domain (**CBZ**):

    – **CBZ-1**: large scar, 70% reduction of g_{Kr}, 80% reduction of g_{Ks};

    – **CBZ-2**: large scar, no reduction of g_{Kr} and g_{Ks}, same values as in healthy tissue;

    – **CBZ-3**: small scar, 70% reduction of g_{Kr}, 80% reduction of g_{Ks}.

Stimulation protocol. S1 stimuli of $250\,mA/cm^3$ amplitude and $5\,ms$ duration are applied

	0D		1D	
	normal	BZ	normal	BZ
$\dot{V}_{max}$ (mV/ms)	289.48	148.00	175.45	76.16
max spike amplitude (mV)	40.98	20.36	21.35	10.63
max dome amplitude (mV)	22.76	9.84	22.67	10.56
APD_{90} (ms)	285.55	303.68	286.95	308.64
APD_{rep} (ms)	279.31	297.38	278.55	298.84

Table 1: Main characteristics of normal and BZ action potentials for a BCL of 500 msec and a stimulus of 50 $mA\,cm^2$, computed from 0D and 1D simulation on a cardiac fiber of length 3 cm with a central BZ region of 1 cm and using a conductivity of 2 $m\Omega^{-1}cm^{-1}$. APD_{rep} is associated to the repolarization time of the inflection in the downstream phase of the AP and APD_{90} is associated to the repolarization time when AP reaches 90% of the resting value during the downstroke phase.

simultaneously at four endocardial apical locations, while S2 stimuli of 1250 mA/cm^3 amplitude and 5 ms duration are applied at an epicardial site located close to the apical entrance of the BZ channel.

In all three simulations settings, the tissue is first paced in the S1 stimulus location for 2000 ms at a basic cycle length (BCL) of 400 ms. In the following, we will denote as S1S2 coupling interval the time interval between the S1 and the S2 stimulations.

2.3.2 Scar with sub-epicardial border zone (EBZ)

Computational domain. We consider here the same LV idealized geometry described previously, discretized by the same finite element grid. The only difference is that the scar region, of dimension about $2 \times 3.5 \times 0.95$ cm^3 (thin case) or $2 \times 3.5 \times 0.75$ cm^3 (thick case), extends from endocardium, along the transmural thickness, up to a sub-epicardial thin BZ region of depth amounting to 0.05 cm (thin case) and 0.25 cm (thick case). This geometrical setting is a schematic representation of a thin sheet of parallel oriented fibers surviving on the epicardial surface, observed in animal experiments, overlying a myocardial infarct induced after complete ligation of the left anterior descending coronary artery [41, 18, 84, 78, 43, 48, 85, 83]. In these experimental studies, the depth of the EBZ ranges between 0.05 and 0.25 cm.

Parameter calibration. In the healthy and scar tissues all parameters are the same used in the channel CBZ simulations. The BZ is modeled as in the **CBZ-1** setting.

Stimulation protocol. Stimulations of 250 mA/cm^3 amplitude and 1 ms duration are applied in a small subendocardial volume located in four different sites depending on the simulation points displayed in Fig. 4:

- Sub-epicardial border zone: left ventricular domain (**EBZ**):

    – **EBZ-A1**: apical stimulation at point A1;
    – **EBZ-A2**: apical stimulation at point A2;
    – **EBZ-M1**: basal stimulation at point M1;
    – **EBZ-M2**: basal stimulation at point M2
    – **EBZ-B1**: basal stimulation at point B1;
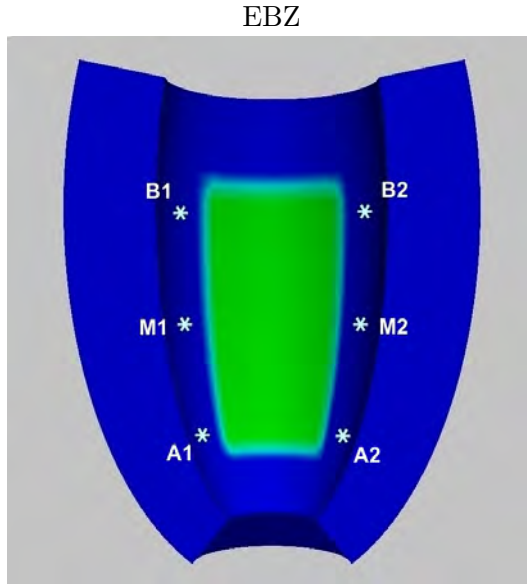   – **EBZ-B2**: basal stimulation at point B2.

EBZ

Figure 4: Endocardial view of EBZ domain with 6 stimulation sites.

The tissue is first paced for $2000\,ms$ at a BCL of $400\,ms$, thus eight S1 stimuli are delivered. Then an S2 stimulus of same amplitude, duration and location of the S1 is applied $320\ ms$ after the last S1. An S3 stimulus is then applied $250\ ms$ after the S2. Eventually, an S4 stimulus is applied $250\ ms$ after the S3.

2.3.3 Post-Processing

In the following, the transmembrane potential maps are displayed not on the computational grid, but on a coarser grid of size $0.8\ mm$. We have also computed the activation time, defined in the general point $\mathbf{x}$ as the unique instant t_A when $v(\mathbf{x}, t_A) = -50\ mV$ during the upstroke phase of the action potential.

3 Results

3.1 Channel border zone, left ventricle (CBZ)

CBZ-1 setting (Figures 5 and 6). A premature S2 stimulus delivered at an S1-S2 coupling interval of $290\,ms$ does not propagate inside the bottom entrance of the BZ channel, close to the apex of the ventricle, because the BZ tissue is still refractory, but it moves around the scar. Then it enters the BZ channel through the top entrance, close to the base of the ventricle, and, since the BZ tissue has now recovered, it propagates through the channel. Eventually the wavefront exits through the bottom gate into the healthy tissue and propagates again around the scar, leading to a stable ventricular tachycardia.

CBZ-2 setting (not shown). The refractoriness of the BZ is almost the same as in the healthy tissue, and reentry does not occur at any S1-S2 coupling interval. Further results show that, with a
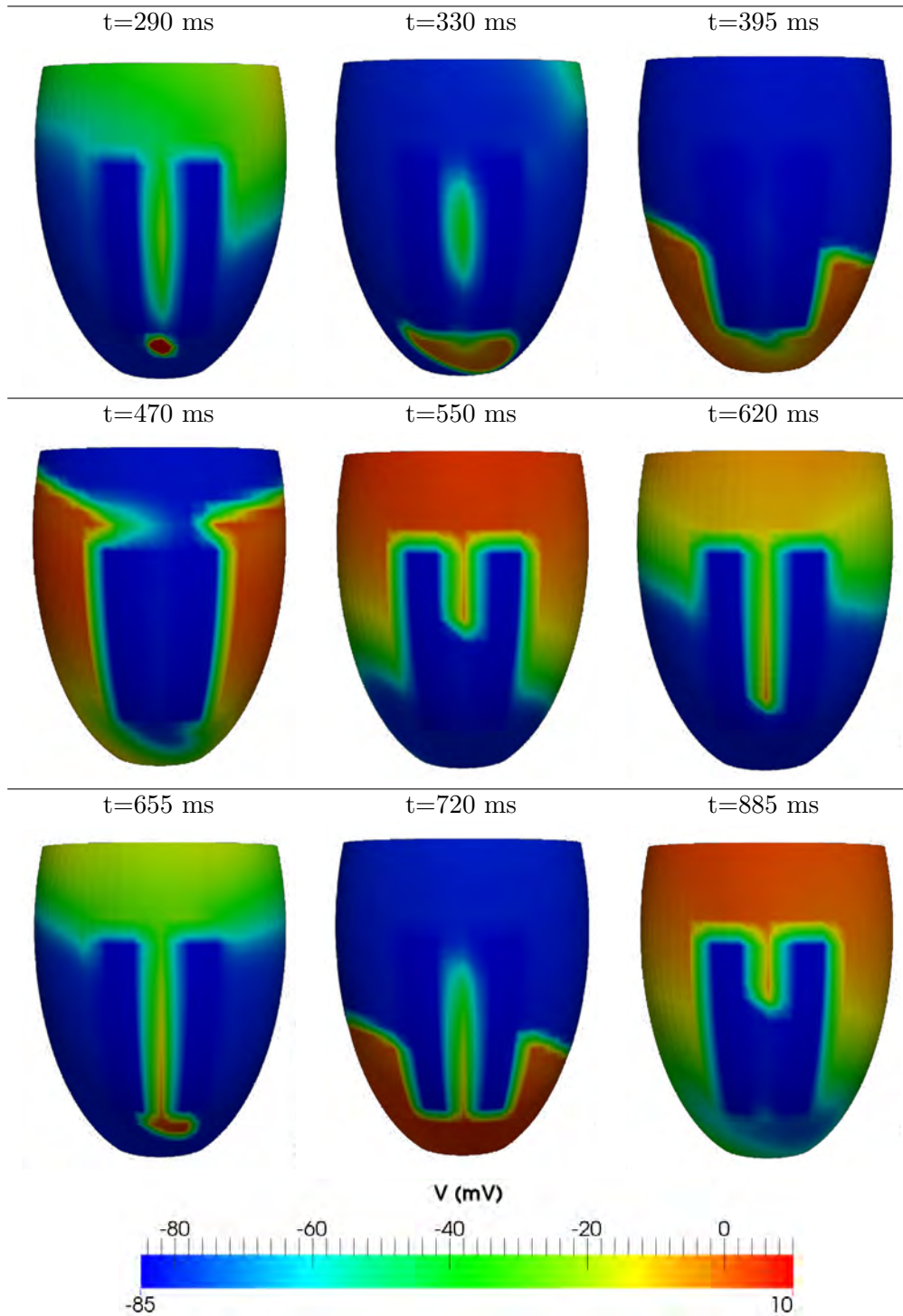
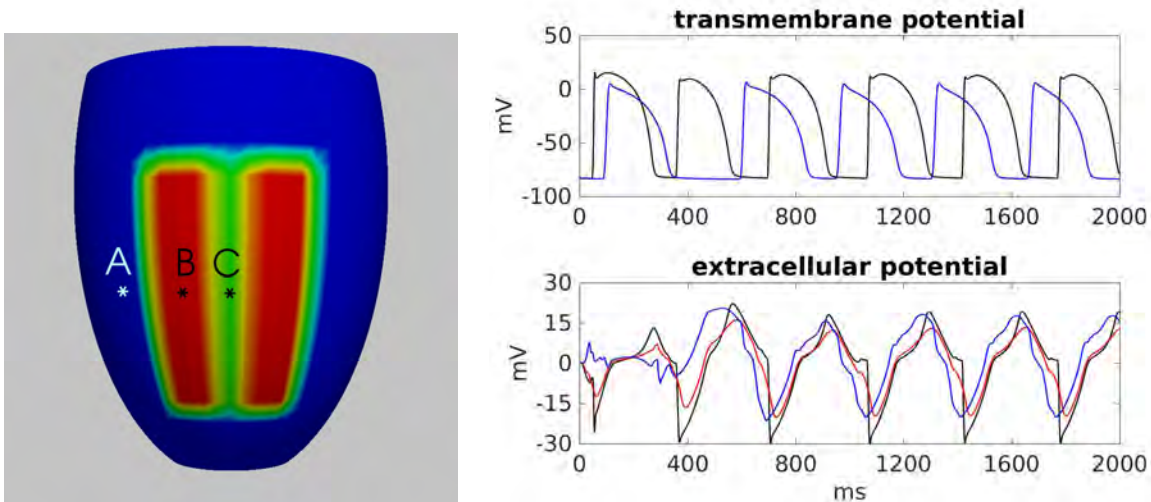Figure 5: **CBZ-1** simulation. Snapshots of transmembrane potential.

Figure 6: **CBZ-1** simulation. **Left panel**. Anterior epicardial view of the idealized left ventricle. The normal tissue is blue, the scar tissue is red, the BZ tissue is green. **Right panel**. Transmembrane and extracellular potential waveforms in three selected points: A (normal tissue, black line), B (scar tissue, red line), C (channel, blue line).

calibration of the g_{Kr} and g_{Ks} BZ parameters intermediate between the **CBZ-1** and **CBZ-2** settings, reentry occurs, but with a reduced vulnerable window with respect to the **CBZ-1** setting.

CBZ-3 setting (Fig. 7). When the scar is small, at S1-S2 coupling intervals between 290 and $300 \, ms$, excitation does not propagate through the bottom gate into the BZ channel but only around the scar. After it has reached the top entrance, the wavefront enters into the BZ channel, which has now recovered, propagates towards the bottom gate, but, when exiting into the healthy tissue, still refractory, it dies. Thus no reentry occurs. For S1-S2 coupling intervals larger that $300 \, ms$, the action potential propagates not only around the scar but also through the bottom gate into the BZ channel, without inducing any reentry.

3.2 Subepicardial border zone, left ventricle (EBZ)

In this set of simulations, we investigate the induction of reentrant ventricular tachycardia in the epicardial border zone (EBZ) overlying the scar region extending up to the endocardial surface, see Figure 2. During an endocardial stimulation, EBZ can not be activated by transmural excitation wavefronts, since the underlying scar is unexcitable, but excitation reaches the epicardium at a breakthrough point located near the EBZ rim connected with the non-infarcted myocardium.

Thin EBZ-M1 simulation (Figures 4 and 8, movie M1_movie.avi in the supplementary material). Fig. 8 reports the snapshots of transmembrane potential starting from $350 \, ms$ after the onset of S3 stimulus ($t = 0$). The S3-S4 coupling interval is $250 \, ms$. After the S4 stimulus, the epicardial activation arises from a breakthrough point ($t = 350 \, ms$) approximately located around the epicardial orthogonal projection of the endocardial stimulation site. The epicardial excitation wavefront moves fast from the epicardial breakthrough and, after reaching the EBZ rim, due to the EBZ refractoriness, initially propagates along the apparent line of functional block composed by the lower and
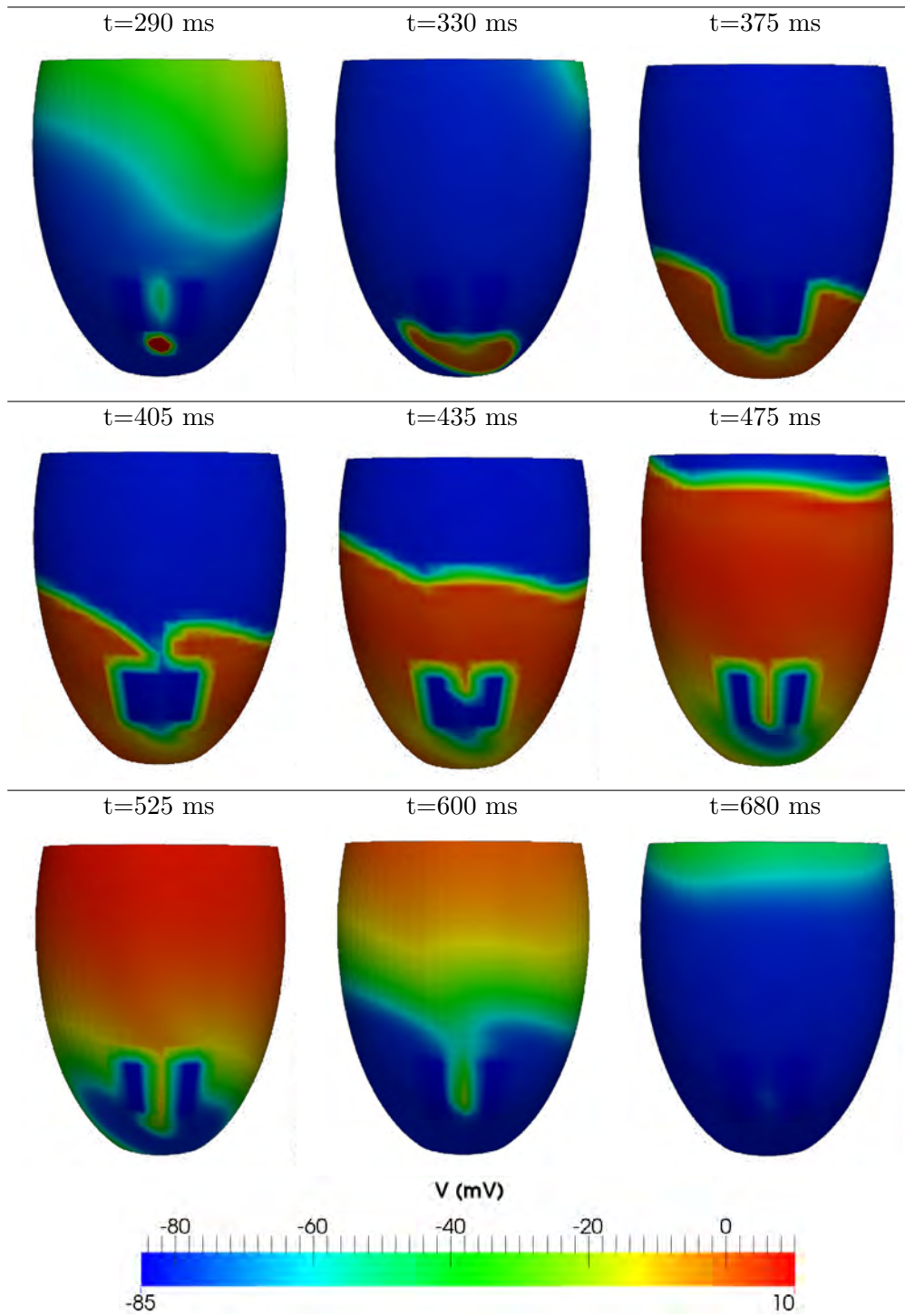
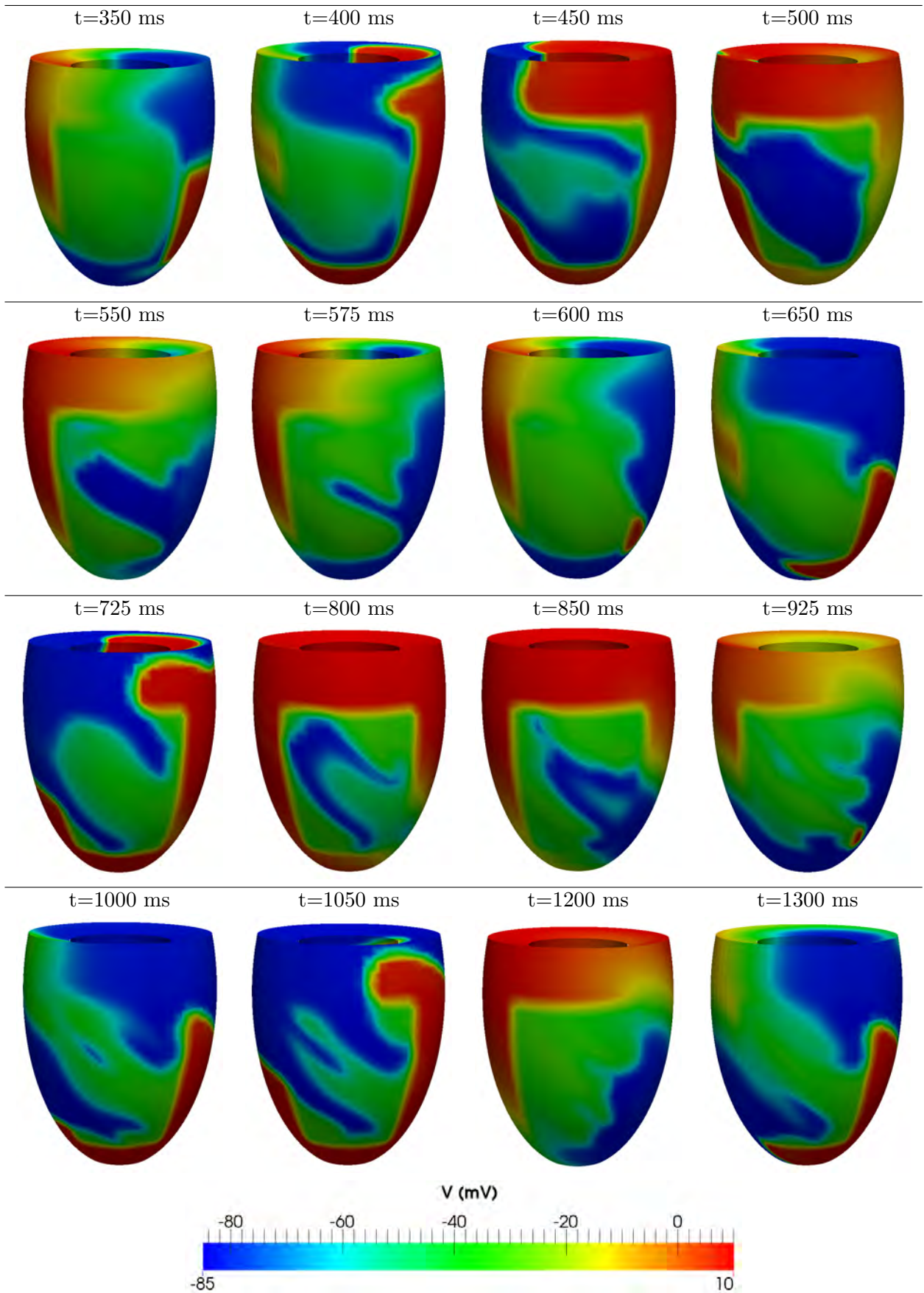Figure 7: **CBZ-3** simulation. Snapshots of transmembrane potential.

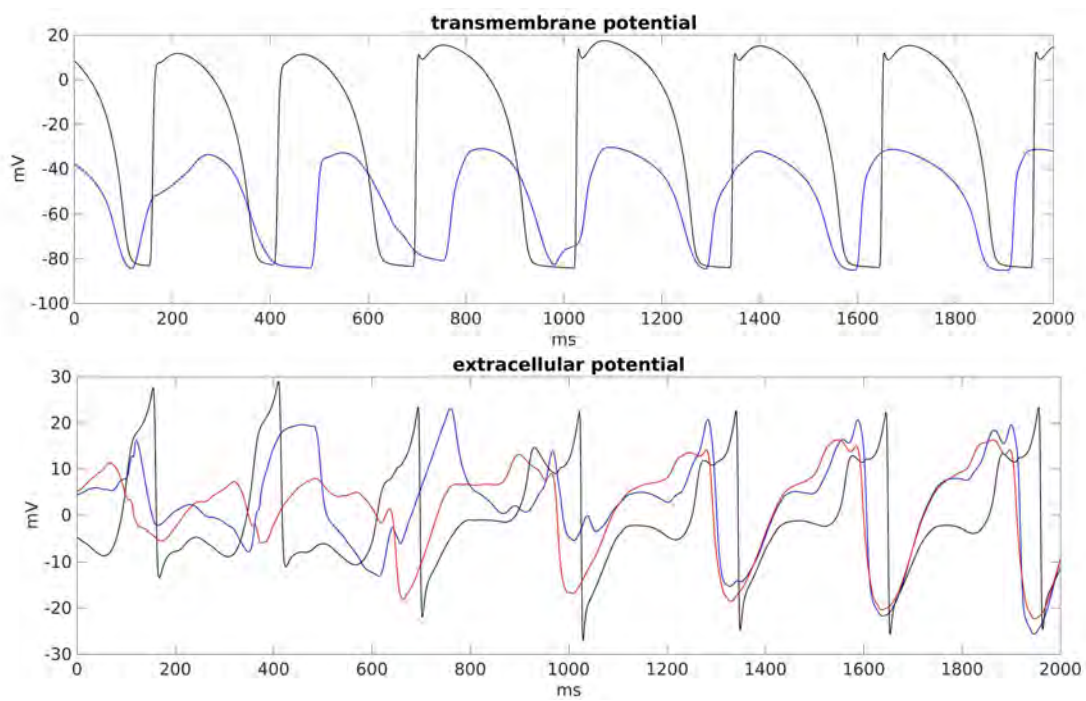Figure 8: EBZ-M1: M1 stimulation site. Snapshots of transmembrane potential.

14

Figure 9: EBZ-M1: M1 stimulation site. Action potentials and electrograms at three selected points in normal tissue (black line), scar tissue (red line) and epicardial border zone (blue line).
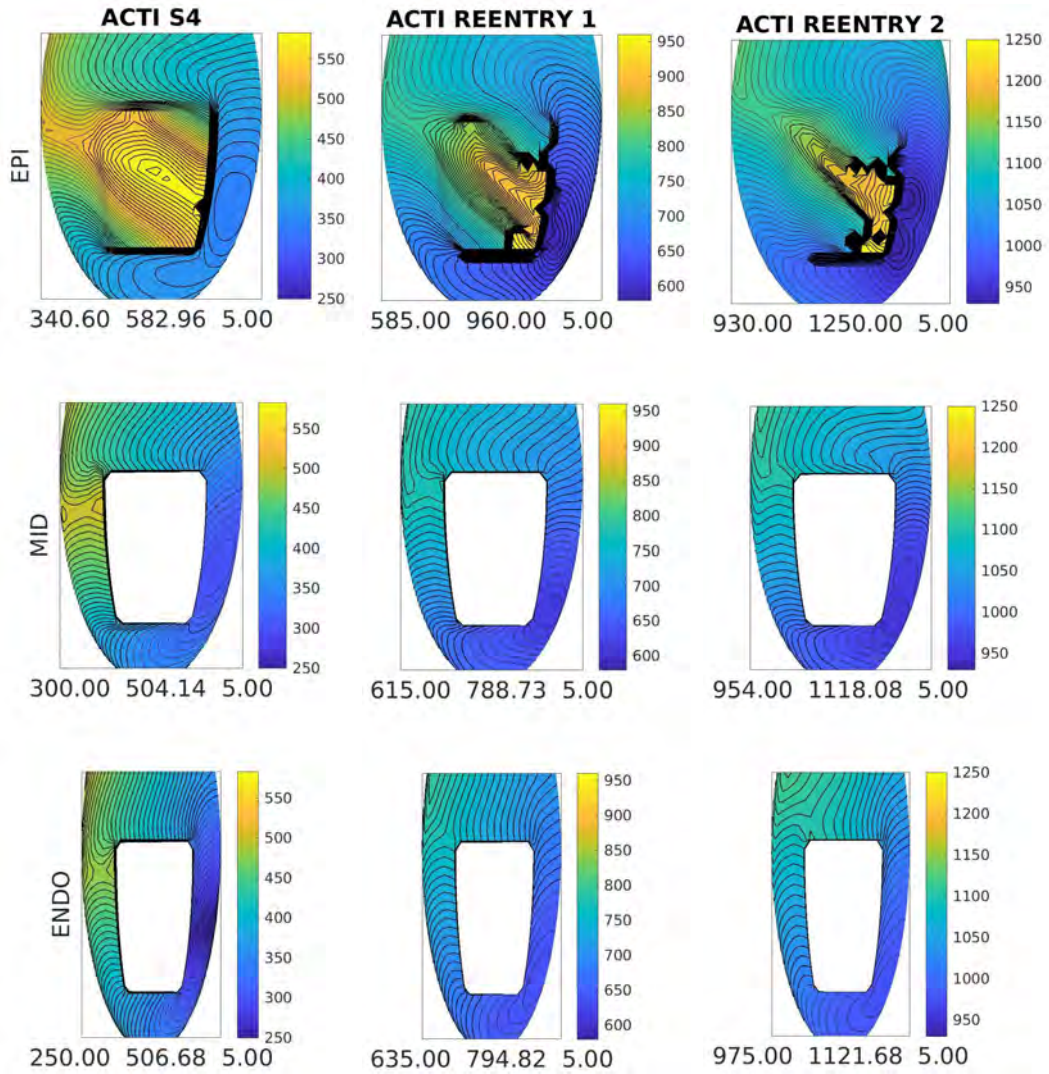
Figure 10: EBZ-M1: M1 stimulation site. Activation time distributions after the S4 stimulus (left), during the first cycle of reentry (center) and during the second cycle of reentry (right) on the epicardial (first row), midmyocardial (second row) and endocardial (third row) surfaces. The three numbers reported below each plot are minimum, maximum and step in ms of the displayed map.
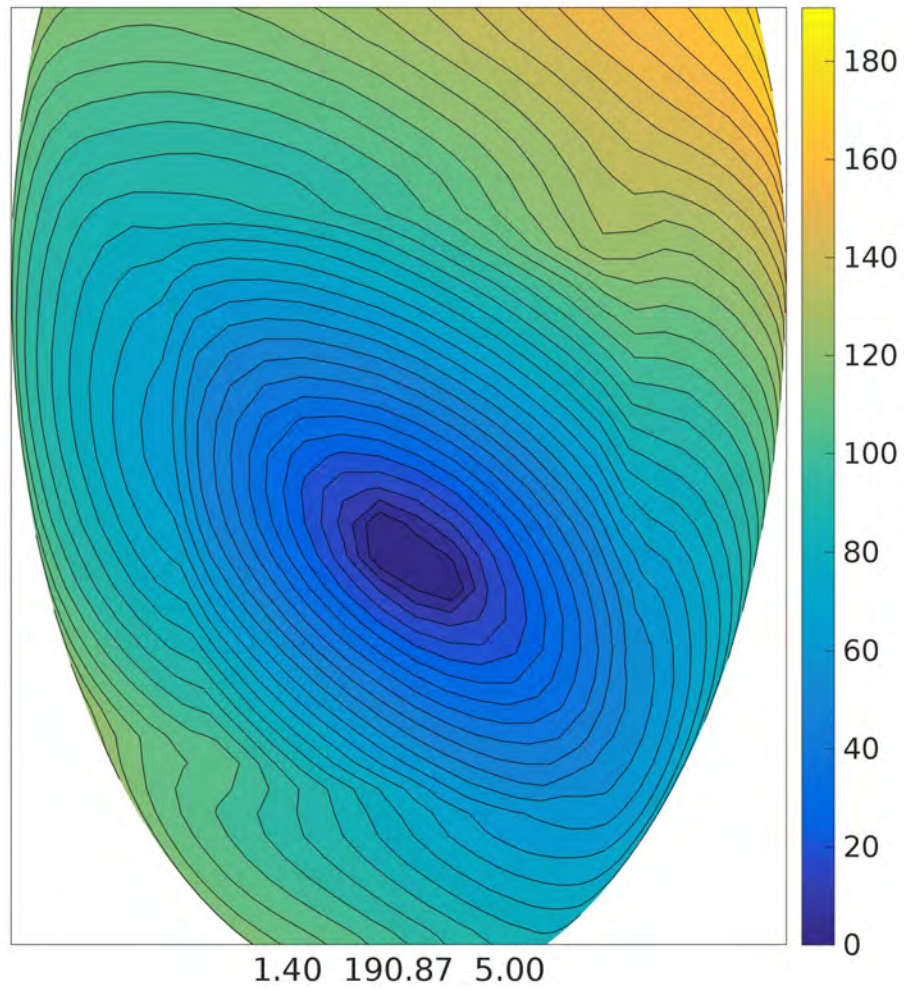
Figure 11: EBZ simulations. Epicardial activation time distribution after a stimulus applied at the center of the EBZ region. The three numbers reported below the plot are minimum, maximum and step in ms of the displayed map.
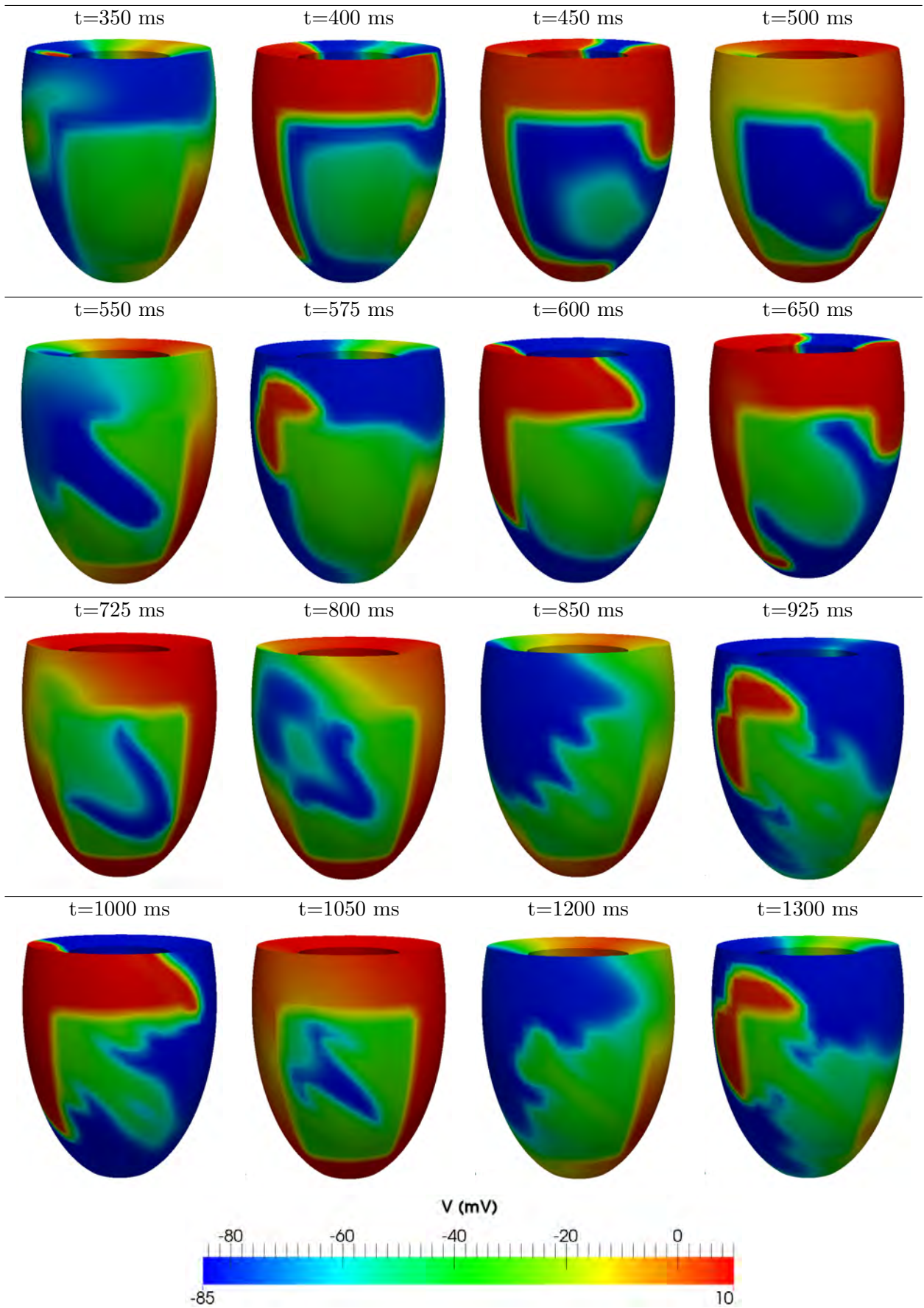
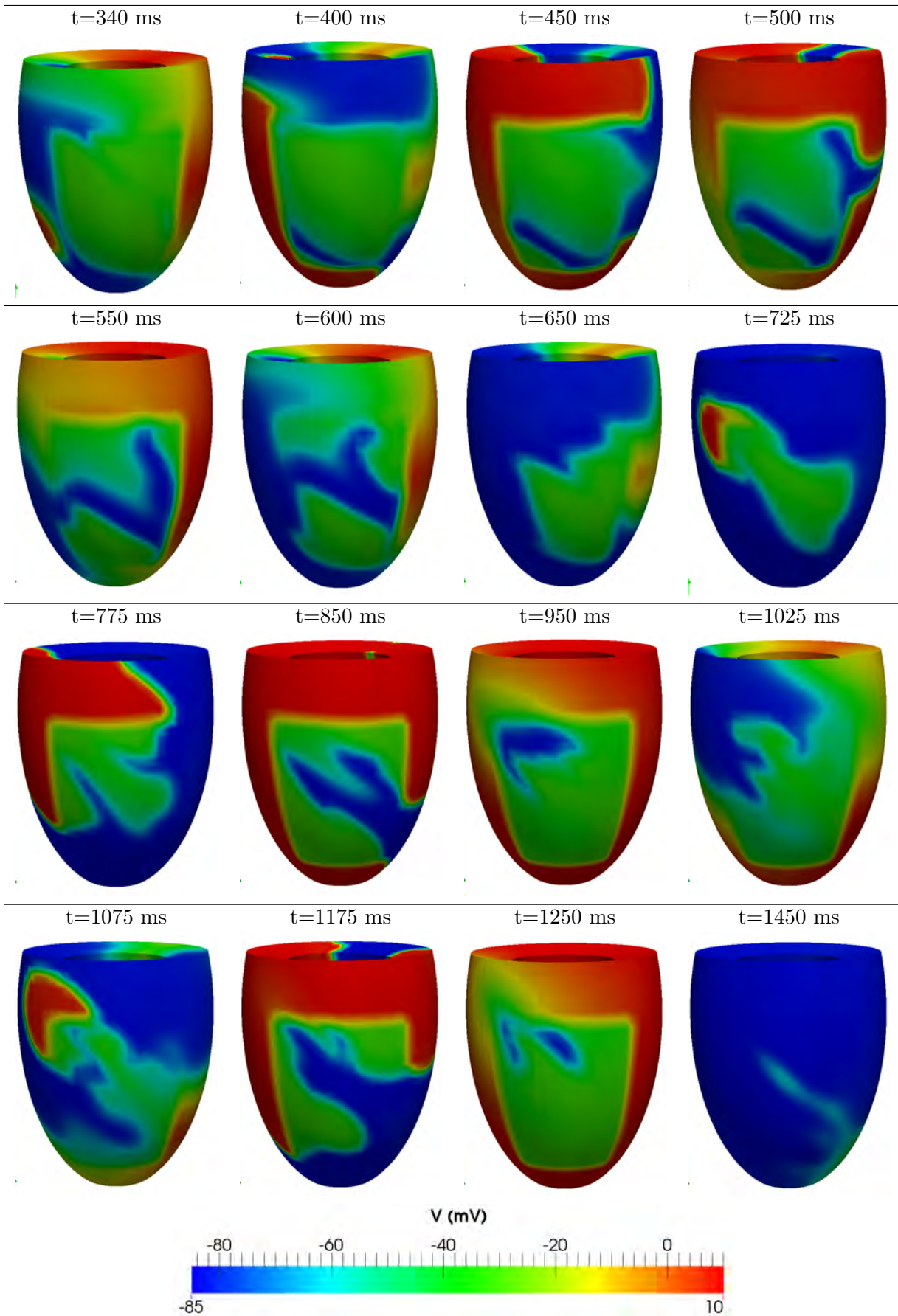Figure 12: EBZ-B2: B2 stimulation site. Snapshots of transmembrane potential.

Figure 13: EBZ-M2: M2 stimulation site, Snapshots of transmembrane potential.

right edges of the EBZ ($t = 400$, $450\ ms$). Subsequently, although the EBZ returns excitable, the L-shaped block persists and excitation propagate along it. Then, excitation turns around both ends of the block line and propagates inside the EBZ ($t = 450$, $500\ ms$), forming two wavefronts moving slowly mainly across the local fiber direction of -45°, from the upper and lower margins of the EBZ. The two wavefronts subsequently merge and excitation proceeds along the fiber direction reaching the bottom right apical part of the EBZ ($t = 600\ ms$) and re-exciting the healthy epicardial tissue and inducing two reentrant waves. Since the EBZ is now refractory, the two reentrant epicardial wavefronts propagate along the L-shaped conduction block, composed by the lower and right edges of the EBZ rim ($t = 650$, $725\ ms$). When the EBZ is again excitable, since the L-shaped conduction block remains, the excitation wavefronts propagate inside the EBZ moving across fiber and issuing from the end points of the L-shaped block line ($t = 800\ ms$). After the wavefronts merge, excitation reaches the bottom right apical part of the EBZ ($t = 925\ ms$), re-exciting the normal epicardial tissue and inducing the second reentrant pathway. This type of cycle of reentry becomes stable and is maintained during the entire simulation time of $4\ s$ as in a sustained ventricular tachycardia; see the transmembrane and extracellular potential waveforms reported in Fig. 9.

The excitation sequences related to the S4 stimulus and the first two reentrant beats are displayed in Fig. 10, displaying the isochrones of the activation time distributions associated to the epicardial, midwall and endocardial layers. The characteristics of the isochrone maps confirm the activation dynamics described previously. Note in particular that, after the S4 stimulus, the first activated locations are the endocardial ones around the stimulation point, conversely, in the reentrant beats, the first activated locations are epicardial and close to the right apical boundary of the EBZ region.

The excitation sequence during reentry presents two black lines corresponding to the line of apparent block along the edges of the EBZ. These lines are formed by linear interpolation of a large number of isochrones between adjacent sites at which activation times might differ more than 100 ms. As usual convention, the thick black line, appearing in the isochrones sequence and resulting from interpolation, is interpreted as an indication of conduction block, but it can indicate a very slow excitation and therefore it can be considered as a *line of apparent (or functional) block*. Indeed it is not caused by any anatomical obstacle, but it mostly results from the functional properties of the cardiac muscle.

To highlight the conduction properties of the EBZ region, we have considered the excitation sequence elicited by a stimulus applied at the center of the EBZ area, see Fig. 11. Inside the EBZ we have almost no intramural fiber rotation due to the thin intramural thickness of the EBZ ($0.05\ cm$) as confirmed by the pattern of elliptical isochrones. When the excitation reaches the EBZ rim encountering the normal myocardial tissue, propagation moves faster both along and across the local epicardial fiber direction with the appearance of two bulges of fast spreading reflecting the underlying counter-clock-wise intramural fiber rotation. We remark that inside the EBZ the joint role of the reduction of I_{Na} current and of conductivity coefficient across fiber causes a decrease of the propagation velocity especially when excitation moves transversely to the fiber direction, but no lines of conduction block appear near the EBZ rim connected with the normal myocardial tissue.

Thin EBZ-B2 simulation (Figures 4 and 12, movie B2_movie.avi in the supplementary material). In case of **B2** stimulation site indicated in Fig. 4, the epicardial breakthrough of the excitation wavefront elicited from the S4 stimulus appears close to the left basal boundary of the EBZ ($t = 350\ ms$). As in the EBZ-M1 case, the EBZ is still refractory, hence the wavefront spreads first along the apparent L-shaped line of conduction block, composed by the left and upper edges of the EBZ ($t = 400\ ms$). Then, at $t = 450\ ms$, although excitability inside the EBZ is clearly restored, the

L-shaped conduction block persists, pointing out insufficient electrotonic currents required to sustain propagation along fiber through the EBZ region. Therefore, excitation spreads along the L-shaped block until it turns around the ends of the block line and propagates inside the EBZ forming two wavefronts moving across fiber, which subsequently merge. The resulting excitation wave reaches the top left basal part of the EBZ ($t = 575\ ms$), reactivating the healthy epicardial tissue and inducing reentry. At ($t = 600\ ms$), due to the refractoriness inside the EBZ, the L-shaped conduction block occurs again and propagation moves along the L-shaped profile. When excitation reaches and turns around the L-shaped end points, being excitability restored inside the EBZ, two wavefronts propagate across fiber and subsequently collide ($t = 650,\ 725,\ 800,\ 850\ ms$). Eventually, excitation proceeds towards the left and upper vertex of the EBZ rim and reactivates again epicardial sites in the normal tissue, triggering the second cycle of reentry ($t = 925\ ms$), which results in a reentrant sustained ventricular tachycardia. In this case too, the pattern of the cycle of reentry maintains during the whole simulation time of $4\ ms$.

Thin EBZ-M2 simulation (Figures 4 and 13). The epicardial breakthrough, related to the excitation wavefront elicited by the S4 endocardial stimulation at site M2, is located near the left apical boundary of the EBZ ($t = 340\ ms$). As in the previous cases, initially the EBZ is still refractory and excitation propagates around an apparent L-shaped block line composed by the lower and left edges of the EBZ ($t = 400\ ms$). Between $t = 400\ ms$ and $t = 450\ ms$, we observe that, while the upper EBZ region remains refractory and the excitation wavefront propagates along the upper EBZ edge, near the lower part of the EBZ rim excitabilty is restored and from the left-lower vertex a sufficient electrotonic current is available to sustain propagation across fiber. Then, between $t = 500\ ms$ and $t = 550\ ms$, excitation turns around the ends of the block line, but at the same time from left-lower and right-upper vertexes of the EBZ rim two wavefronts propagate through the EBZ, become excitable again. Subsequently, these wavefronts collide and propagation proceeds towards the top left basal vertex of the EBZ rim ($t = 725\ ms$). Then, it reexcites the healthy epicardial tissue and induces reentry. At $t = 775\ ms$, an L-shaped block line, composed by the upper and left edges of EBZ rim, is established due to the EBZ refractoriness. Subsequently, after excitation turns around the end points of the L-shaped line, from these sites two excitation wavefronts arise and propagate inside the EBZ region, then colliding ($t = 850\ ms$ and $t = 950\ ms$). The activation of the EBZ region proceeds by pointing towards the left upper vertex of the EBZ rim ($t = 1025\ ms$), re-activating sites in the normal epicardial tissue and forming again a cycle of reentry, but, differently from the EBZ-M1 and EBZ-B2 settings, here only two reentrant cycles occur, since excitation dies at about $1400\ ms$.

Thin EBZ-A1 simulation (Figure 4). In this case, the entire dynamics is similar to the EBZ-M1 simulation, but, instead of a maintained VT, only four reentrant cycles occur, and then excitation dies at about $1950\ ms$ (not shown).

Thin EBZ-B1 and **EBZ-A2 simulations** (Figure 4). In this case, only one reentry occurs after the S4 stimulus (not shown).

Summarizing, in case of thin EBZ, we have detected the following number of cycles of reentry:

- for B2 and M1 stimulation sites, we have sustained reentry observed until $4\ s$ with 11 cycles of reentry;
- for A1 stimulation site, we have 4 cycles of reentry;
- for B1 stimulation site, we have only 1 cycle of reentry;
- for M2 stimulation site, we have 3 cycles of reentry;
- for A2 stimulation site, we have no reentry.

Moreover, these cycles of reentry share the following characteristics:

- the reentrant pathway develops always along the epicardial fiber direction;

- the exit site from the EBZ of the reentrant wavefront is located near the lower-right or upper-left EBZ vertex, depending on the initial stimulation site.

We remark that, we have modeled the EBZ preserving the normal fiber direction, only with reduced across fiber conductivity. Therefore no subepicardial channels are present. Nevertheless, the detected reentrant pathway, developing along the fiber direction, realizes a type of functional channel.

Thick EBZ. In all previous cases, the EBZ overlying the scar is very thin, with an average thickness of about $0.05\,cm$. We have investigated how the thickness of the EBZ influences the onset of VT. With a thicker EBZ of about $0.25\,cm$, the excitation induced by the premature S4 stimulus does not generate any line of functional block at the EBZ edges, and consequently no reentry is induced, irrespective of the stimulation site.

4   Discussion

Understanding the bioelectrical mechanisms responsible for the onset and maintenance of VT in patients affected from infarct scars has an important clinical interest. In particular, it might help in improving and/or identifying novel arrhythmic risk stratification strategies, which currently are mainly limited to the left ventricle ejection fraction (LVEF) criterion [1]. However, LVEF $< 30-35\%$ has been shown to be a non-specific and non-sensitive criterion for risk evaluation of ventricular tachycardia (VT) [72, 55, 62]. Moreover, unraveling the mechanisms which lead to the genesis of VT might be helpful for the reduction of the time required by invasive procedures to determine the ablation sites.

In the present computational study, we have investigated by means of Bidomain numerical simulations the role of scar extent, of the repolarization properties of scar tissue BZ and of the thickness of the BZ surrounding a necrotic scar volume in the genesis and maintenance of reentrant dynamics mimicking a monomorphic ventricular tachycardia. We confined our investigations to two scenarios:

- **CBZ simulations**: the scar region extends along the entire transmural wall thickness, from endocardium to epicardium, with the exception of a BZ shaped as a central sub-epicardial channel, constituting a transition region of viable myocardium;

- **EBZ simulations**: the scar region extends transmurally along the ventricular wall, from the endocardium until a sub-epicardial surface, and it is surrounded by a BZ region of viable myocytes.

4.1   CBZ simulations

4.1.1   Role of scar dimension in the genesis of VT

The role of scar extent in the genesis of reentrant ventricular tachycardias is confirmed by our study. The scar extent is a crucial element for the genesis of reentry because it conditions the time delay to reach the opposite side of isthmus through the outer loop. This delay ensures the complete repolarization of the group of cells forming a protected isthmus after a functional block of premature ventricular contraction (PVC). This result is supported by previous studies in which

the quantification of myocardial scar burden identifies patients with ICM and NICM who would benefit from ICD implantation [67, 42]. Bello et al. performed a sentinel study demonstrating that the quantification of myocardial scar with late gadolinium enhancement (LGE-MRI) was correlated with the rate of VT inducibility at electrophysiological testing [9]. Klem et al. [47] showed that the extent of total scar (cutoff > 5% LV mass) was the most important parameter to red arrhythmia risk stratification in patients with ICM and NICM and, interestingly enough, similar to the cutoff value of 4.8% by Assomull et al. [6] in NICM cohort. Although speculative, these results suggest that a certain "critical" left ventricular scar volume is necessary to induce reentrant VT. In line with this hypothesis, it is interesting to understand whether a spot distribution of scar, with small islands of scar separated by some amount of viable myocardial tissue, confers the same arrhythmic risk of a single large scar at parity of scar burden. The results also suggest that, when the BZ channel is longer than a critical value, reentrant VT occurs. Moreover, the longer is the channel, the larger is the VT cycle length, resulting in a slower arrhythmia.

4.1.2 Role of refractoriness of border zone isthmus in the genesis of VT

In our study repolarization properties of the isthmus show an important role in the genesis of reentrant VT because of their propensity to give functional blocks or slow conductions. The importance of refractoriness of CBZ was also claimed in a previous computational study [27], which focused in particular on understanding how different model representations of the scar volume might influence the electrophysiological properties of BZ and eventually the induction of reentry. However, heterogeneity in the refractoriness of CBZ is not the only cause of conduction block giving rise to reentry dynamics. In fact a different mechanism, based on the interplay of spontaneous calcium release and fibrosis, has been proposed recently in the simulation study [17]. Several experimental studies have also investigated the cellular properties of BZ tissue. Indeed, growing research interest has been aroused by the BZ because of an alleged correlation with ventricular arrhythmias, appropriate ICD discharge and cardiovascular mortality [34, 86]. Recently, it was shown that LGE-MRI driven infarct tissue heterogeneity is associated with mortality [86] and VT [64]. Histological studies have shown that BZ is composed of an heterogeneous mix of viable myocardium and necrotic scar [4]. These regions have isolated/late, low voltage and fractionated bipolar potentials during sinus/paced rhythm and this activation pattern reflects local slow conduction of these myocytes bundles [71, 11]. These electrophysiologic features could cause conduction blocks of PVC giving rise to reentry. Phenomena of nerve sprouting and heterogeneous hyper-innervation could lead to dispersion of time of repolarization, which could favour reentrant VT [69, 79].

Summarizing, the results of CBZ simulations strengthen the importance of the scar extent and the role of BZ in the likelihood of genesis of reentrant VT. Myocardial tissue characterization with cardiac MRI could play an important role in primary SCD risk stratification, with the analysis of scar burden and scar tissue heterogeneity, in addition to LVEF measurements.

4.2 EBZ simulations

The formation of conduction blocks along the EBZ boundary is a necessary condition for inducing a reentrant pathway. We recall that we have modeled the EBZ tissue with an APD increase (about 20 ms) with respect to the APD of the normal tissue, see Fig. 3 and Table 1. This quite limited APD increase, smaller than that considered in other simulation studies, see e.g. [3, 27, 36], is sufficient to induce conduction blocks at the EBZ rim after the S4 endocardial stimulations.

We analyze and provide an interpretation of the types of conduction blocks, that are established following the S4 stimulus or in reentrant circuits. We study how the conduction blocks are affected by the six different endocardial stimulation sites and the role played by refractoriness, electrotonic current and tissue anisotropy on the genesis and development of the conduction blocks.

4.2.1 Functional conduction block after S4 stimulus

For the M1, A1 and B2 stimulation sites, the S4 stimulus induced an epicardial L-shaped conduction block, formed by two edges of the EBZ rim issuing from the lower-right or the upper-left corner, depending on the stimulation site. The conduction block is due initially to the long refractory period in the EBZ. Then, since the block maintains also after the EBZ has become excitable again, it might be attributed to the insufficient availability of electrotonic current to sustain propagation along the fiber direction, intersecting the L-shaped line at -45°, see Figures 14 and 15. Thus the second part of the conduction block is a merely anisotropic effect. The activation of the EBZ is due to two wavefronts originating from the two opposite vertexes of the EBZ, connected by a line almost orthogonal to the epicardial fiber direction. The propagation of such fronts, transverse to the fibers, is ensured by a sufficient electrotonic current.

We recall that the local source-sink relationship determines the heterogeneity of the propagation and depends on the active and passive properties of the tissue, such as reduced excitability and decreased gap junction coupling, see [46]. In fact, it is well known that the threshold requirements for active propagation are lower for transverse than longitudinal propagation (see e.g. [32]) and that less electrical charge distribution is required to sustain propagation across than along fibers as quantified in term of the so-called *safety factor*; see [68, 65, 46]. For anisotropic propagation, the safety factor is low when moving parallel to the myocardial fibers, i.e. the electrotonic current required to sustain propagation along fiber is higher than the one required across fiber.

In our case, the reduction of the intracellular conductivity transversely to fiber in the EBZ has increased the local safety factor allowing the excitation of the EBZ by means of the two cross fiber propagating wavefronts. On the other hand, no changes are made in the EBZ for the along fiber coupling with respect to the normal tissue, therefore the low source-sink ratio for a propagation along fiber is responsible of the persistence of the L-shaped conduction block inside the thin intramural layer.

Previous experimental studies [49, 38] have shown that the electrotonic current due to anisotropic gradients in transmembrane potentials through boundaries between normal and BZ tissue is an important factor for creating functional conduction blocks in healed ischemic tissue. We remark that the electrotonic current through the boundaries between normal and BZ tissue might also raise the effective refractory period in these regions and thus facilitate conduction blocks of excitation elicited by premature stimuli, see [28].

For the other stimulation sites (B1, M2, A2), the S4 stimulus induced only a partial epicardial L-shaped conduction block, always formed by two edges of the EBZ epicardial boundary issuing from its vertex near the epicardial breakthrough. Since the contiguous EBZ area near the L-shaped lines results recovered, near the vertex a sufficient electronic current, flowing from the excited normal tissue, allows the propagation of an excitation wavefront moving across the epicardial fiber direction. Instead, the other part of the L-shaped block can be attributed partly to EBZ refractoriness and to the inability to propagate the excitation inside the EBZ due to local insufficient source-to sink relationships. As a consequence, also in this case partly of the L-shaped block is determined by the passive anisotropic properties of the EBZ region.
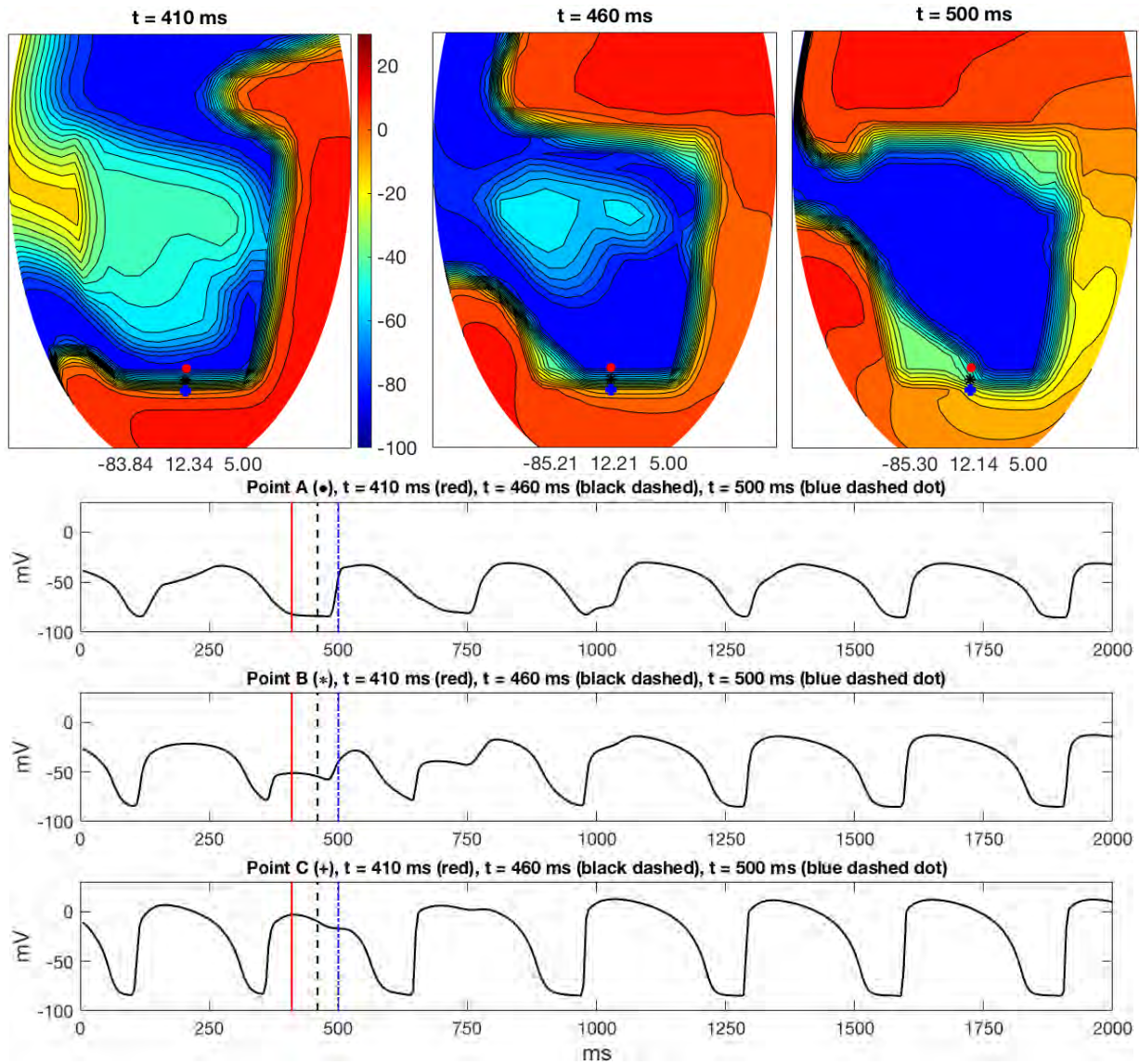
Figure 14: Conduction block after S4 stimulus for M1 stimulation site. Epicardial transmembrane potential distribution at three selected instants and transmemrane potential waveforms taken from three points at the bottom border of the epicardial border zone. The three points A, B and C are labeled as ·, ∗ and +, respectively, in the contour plots.
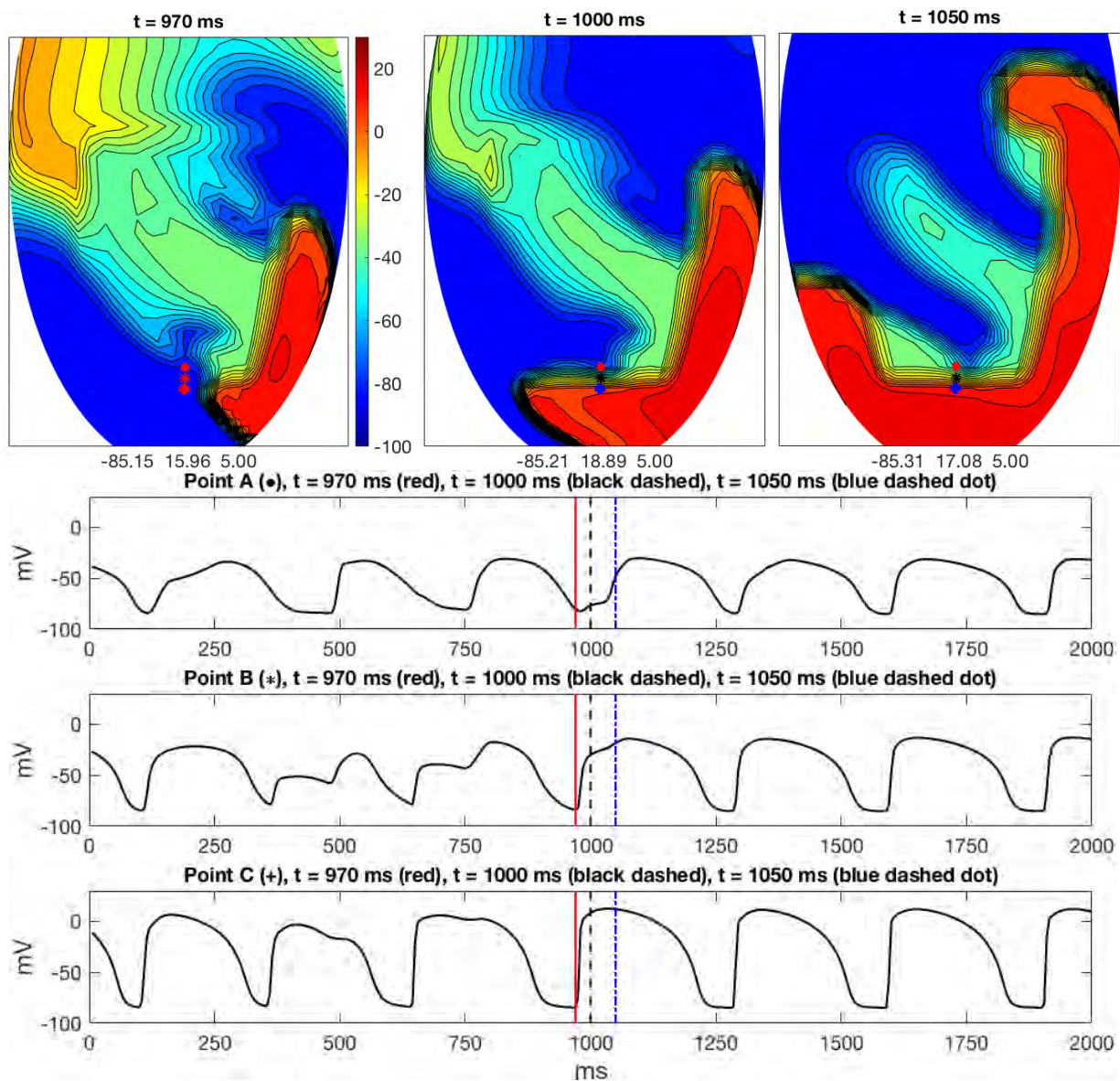
Figure 15: Conduction block during the second cycle of reentry for M1 stimulation site. Epicardial transmembrane potential distribution at three selected instants and transmemrane potential waveforms taken from three points at the bottom border of the epicardial border zone. The three points A, B and C are labeled as ·, * and +, respectively, in the contour plots.

In conclusion, the EBZ simulations suggest that, depending on the endocardial stimulation site, the origin of the epicardial conduction blocks, partially located at the L-shaped EBZ rim, is due to the refractoriness and the low local safety factor of the margins of the EBZ, which do not allow propagation along the fiber direction.

4.2.2 Functional conduction block in cycles of reentry

Concerning the origin of the conduction blocks observed during the reentrant pathways occurring in the EBZ-B2 (EBZ-M1) simulation, they are formed by the two edges issuing from the upper-left (lower-right) vertex of the EBZ epicardial rim and the block is of mixed origin. Initially, the L-shaped block is due to refractoriness of the EBZ region. The block lines develop and persist due to the low safety factor of the anisotropic propagation along fiber, i.e. the electrotonic current flowing from the normal tissue is not sufficient to sustain excitation propagating across the margins of the EBZ. In fact, the recovered EBZ is finally activated by two wavefronts, arising from the end points of the L-shaped block line and propagating slowly across the fiber direction.

Conversely, in the EBZ-B1 (EBZ-M2) simulation during the last cycle of reentry we have initially a bounded epicardial region containing the triggering area located near the lower-right (upper-left) EBZ rim and a not fully recovered part of the EBZ region. Subsequently no epicardial conduction block in the EBZ zone occurs. Therefore the excitation can spread in almost all directions inside the EBZ area, then it collides and the entire EBZ area reaches the resting state, see Fig. 13 (last row).

Summarizing, we have observed the following two different behaviors of the excitation pathways around the EBZ rim during the cycles of reentry:

- for the stimulation sites A1, M1 and B2 of Fig. 4, the excitation wave reaches the EBZ rim moving mainly along the epicardial fiber direction of -45°, but it does not cross it due partly to refractoriness and to an insufficient electrotonic current for the along fiber propagation in the thin layer of the BZ. In these cases, reentry is generally sustained;

- for the stimulation sites B1, M2 and A2 of Fig. 4, the excitation wave reaches the EBZ rim moving mainly across fiber and the functional block does not occur because the electrotonic current is sufficient to support the propagation of excitation in the EBZ. In these cases, reentry is hardly maintained, and excitation dies after few loops.

All the simulated cycles of reentry in the epicardial BZ of the infarct scar can be classified as functional anisotropic reentries, since there are no predetermined anatomical conducting pathways, see [83] and they depend on the orientation and heterogeneities of the electrophysiological properties of the cardiac fibers, see Fig. 16. These anisotropic reentries are of the same type of the reentrant circuits observed in experiments on canine [49, 84, 78, 38, 48, 85, 83] and human myocardial infarction [30, 5, 31].

Since we have modeled EBZ with homogeneous electrophysiological properties, preserving the normal fiber direction, our results show that the presence of EBZ heterogeneities, such as fibrosis, is not a necessary factor to induce anisotropic reentry.

We have also run a simulation (not shown) considering a smooth boundary between the normal tissue and the EBZ, stimulating the tissue from the M1 site, and even in this case reentry occurs and is sustained.
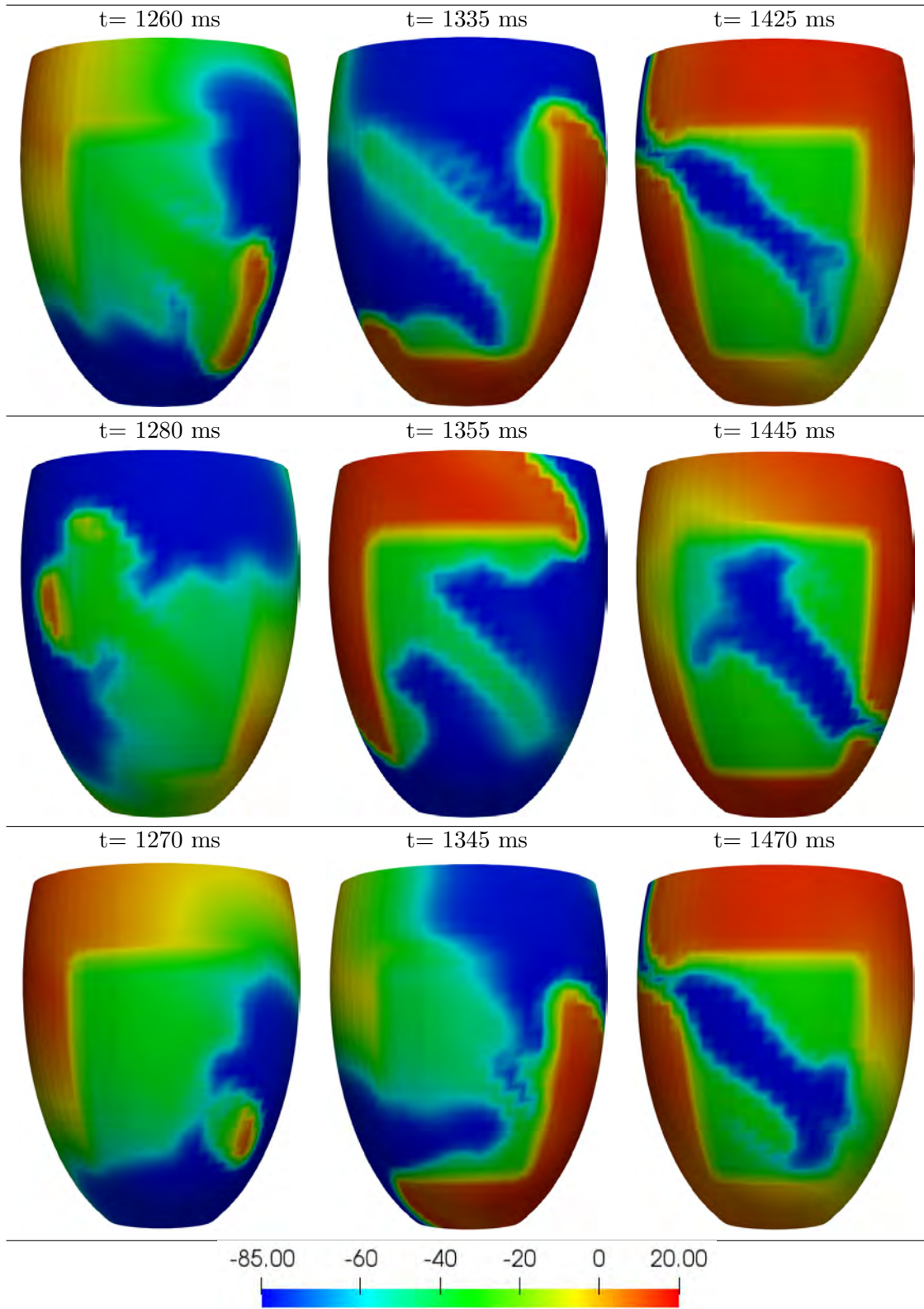
Figure 16: Patterns structure of the third anisotropic cycle of reentry in EBZ-M1 (first row), -B2 (second row) and -A1 (third row) simulations. Snapshots of transmembrane potential at selected instants.

4.2.3 Role of EBZ thickness in the genesis of VT

Another finding emerging from our simulations is that the thickness of EBZ region plays a crucial role in the genesis of VT. With thin EBZ, conduction block occurs after the S4 premature impulse, due to a combination of electrotonic modulation and refractoriness gradient between EBZ and healthy region, and the reentrant wave takes origin. With thick EBZ, conduction block does not occur, and thus reentry is not induced. These results on the role played by the thickness of the subepicardial BZ layer seem to be in partial agreement with the kinetic theory of reentry developed in [20, 21, 22].

Summarizing, an important result of EBZ simulations is the relationship between the site of stimulation and the probability of reentrant VT induction. The anisotropy of cardiac tissue explains this dependence. In our opinion this result could represent one of the reasons of the possible false-negative with programmed ventricular stimulation in primary SCD risk stratification [13, 53, 88].

4.3 Limitations

In CBZ simulations, the isthmus orientation has been chosen arbitrarily and, probably, it might play also a role, because it conditions the critical relation between the conduction time in outer loop of the circuit and the time of cell potential recovery. Moreover, we have not considered BZ tissue around the scar in outer loop to simplify the model and because we suppose that its effect is to accentuate the role of scar dimension in the time delay to reach the opposite side of isthmus.

In EBZ simulations, we have considered a simplified shape of the infarct scar and of the EBZ region, modeled as sectors of the ellipsoidal volume. More realistic scar and BZ shapes should be considered in future studies.

We have considered the presence of homogeneous fibrosis at a macroscopic tissue scale, in particular by reducing the intracellular conductivity across fiber, neglecting heterogeneous modeling of fibrosis.

The modeling of scar and BZ are based on the approach previously published in [7, 3], that was derived from experimental measurements. Alternative approaches to model the scar and BZ regions, for instance the calibration of INa and ICaL currents, might influence the reentrant phenomena. Preliminary results considering the scar as a passive intracellular medium and stimulating the tissue from the M1 site have shown that reentry occurs, but it is not sustained.

5 Conclusion

This study has investigated the dynamics of reentrant ventricular arrhythmias and the importance of electrophysiological property of the border zone and scar extent in their pathophysiology, by means of Bidomain numerical simulations.

In CBZ simulations, the results have shown that:

- the scar extent is a crucial element for the genesis of reentry because it conditions the time delay to reach the opposite side of the channel through the outer loop;

- the repolarization properties of the CBZ, in particular the reduction of IKs and IKr currents, play an important role in the genesis of reentrant VT because of their propensity to give functional block when excitation is elicited by a premature stimulus.

While in CBZ simulations the epicardial BZ wedges between two unexcitable regions and the reentrant pathway is pre-determined, in the EBZ simulations the entire epicardial surface is excitable

and the shape of a possible reentrant cycle is not assigned a-priori. Nevertheless, the results of EBZ simulations have shown that reentry might occur even in this case, and in particular:

- the cycles of reentry always display an excitation pathway in the EBZ which develop along the epicardial fiber direction. All reentrant pathways exhibit the exit site located near the upper-left or lower-right vertex of the EBZ region, depending on the endocardial site of stimulation;

- the propensity and sustainability of cycles of reentry depend on the endocardial stimulation site and on the interplay between the epicardial breakthrough site of excitation, local fiber direction and BZ rim;

- the onset of cycles of reentry depends strongly on the thickness of the subepicardial sheet of parallel-oriented fiber of surviving tissue overlying the scar region.

References

[1] 2016 ESC guidelines for the diagnosis and treatment of acute and chronic heart failure: the task force for the diagnosis and treatment of acute and chronic heart failure of the European Society of Cardiology (ESC). *Europ. Heart J.*, 37: 2129–2200, 2016.

[2] H. Arevalo, G. Plank, P. Helm, H. Halperin and N. A. Trayanova. Tachycardia in post-infarction hearts: insights from 3D image-based ventricular models. *Plos One*, 8 (7): e68872, 2013.

[3] H. J. Arevalo, F. Vadakkumpadan, E. Guallar, A. Jebb, P. Malamas, K. C. Wu and N. A. Trayanova. Arrhythmia risk stratification of patients after myocardial infarction using personalized heart models. *Nature comm.*, 7: 11437, 2016.

[4] H. Arheden, M. Saeed, C. B. Higgins, D. W. Gao, P. C. Ursell, L. Bremerich, R. Wyttenbach, M. W. Dae and R. F. Wendland. Reperfused rat myocardium subjected to various durations of ischemia: estimation of the distribution volume of contrast material with echo-planar MR imaging. *Radiology*, 215 (2): 520-528, 2000.

[5] H. Ashikaga, H. Arevalo, F. Vadakkumpadan, R. C. Blake, J. D. Bayer, S. Nazarian, M. M. Zviman, H. Tandri, R. D. Berger, H. Calkins, D. A. Herzka, N. A. Trayanova and H. R. Halperin. Feasibility of image-based simulation to estimate ablation target in human ventricular arrhythmia. *Heart Rhythm*, 10 (8): 1109–1116, 2013.

[6] R. G. Assomull, S. K. Prasad, J. Lyne, G. Smith, E. D. Burman, M. Khan, M. N. Sheppard, P. A. Poole–Wilson and D. J. Pennell. Cardiovascular magnetic resonance, fibrosis, and prognosis in dilated cardiomyopathy. *J. Am. Coll. Cardiol.*, 48 (10): 1977–1985, 2006.

[7] S. Baba, W. Dun, C. Cabo and P. A. Boyden. Remodeling in cells from different regions of the reentrant circuit during ventricular tachycardia. *Circulation*, 112: 2386–2396, 2005.

[8] S. Balay, S. Abhyankar, M. F. Adams, J. Brown, P. Brune, K. Buschelman, L. Dalcin, V. Eijkhout, W. D. Gropp, D, Kaushik, M, G. Knepley, L. C. McInnes, K. Rupp, B. F. Smith, S. Zampini, H. Zhang and H. Zhang. *PETSc users manual*, Tech. Rep. ANL-95/11 - Revision 3.7, Argonne National Laboratory, 2016.

[9] D. Bello, D. S. Fieno, R. J. Kim, S. Pereles, R. Passman, G. Song, A. H. Kadish and J. J. Goldberger. Infarct morphology identifies patients with substrate for sustained ventricular tachycardia. *J. Am. Coll. Cardiol.*, 45: 1104–1108, 2005.

[10] M. J. Bishop, E. J. Vigmond, and G. Plank The functional role of electrophysiological heterogeneity in the rabbit ventricle during rapid pacing and arrhythmias *Am. J. Physiol. Heart. Circ. Physiol.* 304: H1240H1252, 2013.

[11] F. Bogun, B. Bender, Y. G. Li, G. Groenefeld, S. H. Hohnloser, F. Pelosi, B. Knight, S. A. Strickberger and F. Morady. Analysis during sinus rhythm of critical sites in reentry circuits of postinfarction ventricular tachycardia. *J. Interv. Card. Electrophysiol.*, 7: 95–103, 2002.

[12] D. R. Bolick, D. B. Hackel, K. A. Reimer and R. E. Ideker. Quantitative analysis of myocardial infarct structure in patients with ventricular tachycardia. *Circulation*, 74 (6): 1266–1279, 1986.

[13] J. P. Bourke, A. B. David, D. A. B. Richards, D. L. Ross, E. M. Wallace, M. A. McGuire and J. B. Uther. Routine programmed electrical stimulation in survivors of acute myocardial infarction for prediction of spontaneous ventricular tachyarrhythmias during follow-up: results, optimal stimulation protocol and cost-effective screening. *Am. Coll. Cardiol.* ,18 (3): 780–781, 1991.

[14] C. Cabo and P. A. Boyden. Electrical remodeling of the epicardial border zone in the canine infarcted heart: a computational analysis. *Am. J. Physiol. Heart Circ. Physiol.*, 284: H372–H384, 2003.

[15] C. Cabo, J. A. Yao, P. A. Boyden, S. Chen, W. Hussain, H. S. Duffy, E. J. Ciaccio, N. S. Peters and A. L. Wit. Heterogeneous gap junction remodeling in reentrant circuits in the epicardial border zone of the healing canine infarct. *Cardiovasc. Res.*, 72: 241–249, 2006.

[16] C. Cabo. Dynamics of propagation of premature impulses in structurally remodeled infarcted myocardium: a computational analysis. *Front. Physiol.*, 5: 483, 2014.

[17] F. O. Campos, Y. Shiferaw, R. Weber dos Santos, G. Plank and M. J. Bishop. Microscopic isthmuses and fibrosis within the border zone of infarcted hearts promote calcium-mediated ectopy and conduction block. *Front. Physiol.*, 6: 57, 2018.

[18] R. Cardinal, M. Vermuelen, M. Shenasa, F. Roberge, P. Page, F. Helie and P. Savard. Anisotropic conduction and functional dissociation of ischemic tissue during reentrant ventricular tachycardia in canine myocardial infarction. *Circulation*, 77 (5): 1162–1176, 1988.

[19] R. H. Clayton and A. V.Holden. Computational framework for simulating the mechanisms and ECG of reentrant ventricular fibrillation. *Physiol. Meas.*, 23: 707–726, 2002.

[20] E. J. Ciaccio, A. W. Chow, D. W. Davies, A. L. Wit and N. S. Peters. Localization of the isthmus in reentrant circuits by analysis of electrograms derived from clinical noncontact mapping during sinus rhythm and ventricular tachycardia. *J. Cardiovasc. Electrophysiol.*, 15: 27–36, 2004.

[21] E. J. Ciaccio, H. Ashikaga, R. A. Kaba, D. Cervantes, B. Hopenfeld, A. L. Wit, N. S. Peters, E. R. McVeigh, H. Garan and J. Coromilas. Model of reentrant ventricular tachycardia based on infarct border zone geometry predicts reentrant circuit features as determined by activation mapping. *Heart Rhythm*, 4: 1034–1045, 2007.

[22] E. J. Ciaccio, J. Coromilas, H. Ashikaga, D. O. Cervantes, A. L. Wit, N. S. Peters, E. R. McVeigh and H. Garan. Model of unidirectional block formation leading to reentrant ventricular tachycardia in the infarct border zone of postinfarction canine hearts. *Comput. Biol. Med.*, 62: 254–263, 2015.

[23] P. Colli Franzone, L. Guerri and S. Tentoni. Mathematical modeling of the excitation process in myocardial tissue: influence of fiber rotation on wavefront propagation and potential field. *Math. Biosci.*, 101 (2): 155–235, 1990.

[24] P. Colli Franzone, L. F. Pavarino and S. Scacchi. Exploring anodal and cathodal make and break cardiac excitation mechanisms in a 3D anisotropic bidomain model. *Math. Biosci.*, 230 (2): 96–114, 2011.

[25] P. Colli Franzone, L. F. Pavarino and S. Scacchi. A comparison of coupled and uncoupled solvers for the cardiac bidomain model. *ESAIM Math. Mod. Numer. Anal.*, 47: 1017–1035, 2013.

[26] P. Colli Franzone, L. F. Pavarino and S. Scacchi, *Mathematical Cardiac Electrophysiology,* Springer, MSA Vol. 13, New York, 2014.

[27] A. J. Connolly and M. J. Bishop. Computational representations of myocardial infarct scars and implications for arrhythmogenesis. *Clin. Med. Ins.-Cardiol.*, 10 (1): 27–40, 2016.

[28] A. Connolly, M. L. Trew, B. H. Smaill, G. Plank and M. J. Bishop. Local gradients in electrotonic loading modulate the local effective refractory period: implications for arrhythmogenesis in the infarct border zone. *IEEE Trans. Biomed. Eng.*, 62 (9): 2251–2259, 2015.

[29] J. M. de Bakker, F. J. van Capelle, M. J. Janse, S. Tasseron, J. T. Vermeulen, N. de Jonge and J. R. Lahpor. Slow conduction in the infarcted human heart. 'Zigzag' course of activation. *Circulation*, 88 (3): 915–926, 1993.

[30] C. de Chillou, D. Lacroix, D. Klug, I. Magnin-Poull, C. Marquié, M. Messier, M. Andronache, C. Kouakam, N. Sadoul J. Chen, E. Aliot and S. Kacet. Isthmus characteristics of reentrant ventricular tachycardia after myocardial infarction. *Circulation*, 105: 726–731, 2002.

[31] C. de Chillou, L. Groben, I. Magnin-Poull, M. Andronache, M. Magdi Abbas, N. Zhang, A. Abdelaal, S. Ammar, J. Sellal, J. Schwartz, B. Brembilla-Perrot, E. Aliot and F. E. Marchlinski. Localizing the critical isthmus of postinfarct ventricular tachycardia: The value of pace-mapping during sinus rhythm. *Heart Rhythm*, 11: 175–181, 2014.

[32] C. Delgado, B. Steinhaus, M. Delmar, D. R. Chialvo and J. Jalife. Directional differences in excitability and margin of safety for propagation in sheep ventricular epicardial muscle. *Circ Res.*, 67 (1): 97–110, 1990.

[33] D. Deng, H. Arevalo, F. Pashakhanloo, A. Prakosa, H. Ashikaga, E. McVeigh, H. Halperin and N. A. Trayanova. Accuracy of prediction of infarct-related arrhythmic circuits from image-based models reconstructed from low and high resolution MRI. *Front. Physiol.*, 6: 282, 2015.

[34] S. de Haan, T. A. Meijers, P. Knaapen, A. M. Beek, A. C. van Rossum and C. P. Allaart. Scar size and characteristics assessed by CMR predict ventricular arrhythmias in ischaemic cardiomyopathy: comparison of previously validated models. *Heart.*, 97: 1951–1956, 2011.

[35] K. F. Decker and Y. Rudy. Ionic mechanisms of electrophysiological heterogeneity and conduction block in the infarct border zone. *Am. J. Physiol. Heart Circ. Physiol.*, 299: H1588–H1597, 2010.

[36] D. D. Deng, H. J. Arevalo, A. Prakosa, D. J. Callans and N. A. Trayanova. A feasibility study of arrhythmia risk prediction in patients with myocardial infarction and preserved ejection fraction. *Europace*, 18 (4): 60–66, 2016.

[37] S. de Jong, T. A. B. van Veen, H. V. M. van Rijen and J. M. T. de Bakker. Fibrosis and cardiac arrhythmias. *J. Cardiovasc. Pharm.*, 57: 630–638, 2011.

[38] S. M. Dillon, M. A. Allessie, P. C. Ursell and A. L. Wit. Infuences of anisotropic tissue structure on reentrant circuits in the epicardial border zone of subacute canine infarcts. *Circ. Res.*, 63, 182–206, 1988.

[39] W. Dun, S. Baba, T. Yagi and P. A. Boyden. Dynamic remodeling of K^+ and Ca^{2+} currents in cells that survived in the epicardial border zone of canine healed infarcted heart. *Am. J. Physiol. Heart Circ. Physiol.*, 287: H1046–H1054, 2004.

[40] S. Dutta , A. Mincholè, E. Zacur, T. A. Quinn , P. Taggart and B. Rodriguez. Early afterdepolarizations promote transmural reentry in ischemic human ventricles with reduced repolarization reserve. *Progr. Biophys. Molec. Biol.*, 12: 236–248, 2016.

[41] N. El-Sherif, B. J. Scherlag, R. Lazzara and R. R. Hope. Re-entrant ventricular arrhythmias in the late myocardial infarction period. 1. Conduction characteristics in the infarct zone. *Circulation*, 55: 686–702, 1977.

[42] P. Gao, R. Yee, L. Gula, A. D. Krahn, A. Skanes, P. Leong–Sit, G. J. Klein, J. Stirrat, N. Fine, L. Pallaveshi, G. Wisenberg, T. R. Thompson, F. Prato, M. Drangova and J. A. White. Prediction of arrhythmic events in ischemic and dilated cardiomyopathy patients referred for implantable cardiac defibrillator: evaluation of multiple scar quantification measures for late gadolinium enhancement magnetic resonance imaging. *Circ. Cardiovasc. Imaging*, 5 (4): 448–456, 2012.

[43] W. B. Gough, R. Mehra, M. Restivo, R. H. Zeiler and N. El-Sherif. Reentrant ventricular arrhythmias in the late myocardial infarction period in the dog. 13. Correlation of activation and refractory maps. *Circ. Res.*, 57: 432–442, 1985.

[44] C. S. Henriquez. Simulating the electrical behavior of cardiac tissue using the bidomain model. *Crit. Rev. Biomed. Eng.*, 21: 1–77, 1993.

[45] H.V. Huikuri, J.M. Tapanainen, K. Lindgren, P. Raatikainen, T. H. Mkikallio, K.E.J. Airaksinen, R.J. Myerburg. Prediction of sudden cardiac death after myocardial infarction in the beta-blocking era. J Am Coll Cardiol., 42(4):652658, 2003.

[46] A. G. Kleber and Y. Rudy. Basic mechanisms of cardiac impulse propagation and associated arrhythmias. *Physiol. Rev.*, 84: 431–488, 2004.

[47] I. Klem, J. W. Weinsaft, T. D. Bahnson, D. Hegland, H. W. Kim, B. Hayes, M. A. Parker, R. M. Judd and R. J. Kim. Assessment of myocardial scarring improves risk stratification in patients evaluated for cardiac defibrillator implantation. *J. Am. Coll. Cardiol.*, 60 (5): 408–420, 2012.

[48] M. J. Janse and A. L. Wit. Electrophysiological mechanisms of ventricular arrhythmias resulting from myocardial ischemia and infarction. *Physiol. Rev.*, 69 (4): 1989–1169, 1989.

[49] M. J. Janse, F. J. L. Van Capelle, H. Morsink, A. G. Kleber, F. J. G. Wilms-Schopman, R. Cardinal, C. Naumann d'Alnoncourt and D. Durrer. Flow of "injury" current and patterns of excitation during early ventricular arrhythmias in acute regional myocardial ischemia in isolated porcine and canine hearts. Evidence for 2 different arrhythmogenic mechanisms. *Circ. Res.*, 47: 151–165, 1980.

[50] M. Jiang, C. Cabo, J. Yao, P. Boyden and G. Tseng. Delayed rectifier K currents have reduced amplitudes and altered kinetics in myocytes from infarcted canine ventricle. *Cardiovasc. Res.*, 48: 34–43, 2000.

[51] S. C. Latet, V. Y. Hoymans, P. L. Van Herck and C. J. Vrints. The cellular immune system in the post-myocardial infarction repair process. *Int. J. Cardiol.*, 179: 240–247, 2015.

[52] W. M. Lue and P. A. Boyden. Abnormal electrical properties of myocytes from chronically infarcted canine heart. Alterations in Vmax and the transient outward current. *Circulation*, 85: 1175–1188, 1992.

[53] R. Martinez-Rubio, A. Stachowitz, M. Borggrefe, L. Reinhardt, A. Cabrera-Santos, X. Chen, S. Willems, M. Shenasa and G. Breithardt. Comparison of the results of programmed ventricular stimulation from the right ventricular apex and outflow tract: a randomized, prospective study. *Eur Heart J.*, 16 (9): 1234–1243, 1995.

[54] K. S. McDowell, H. J. Arevalo, M. M. Maleckar and N. A. Trayanova. Susceptibility to arrhythmia in the infarcted heart depends on myofibroblast density. *Biophys J.*, 101 (6): 1307–1315, 2011.

[55] A. J. Moss, H. Greenberg, R. B. Case, W. Zareba, W. J. Hall, M. W. Brown, J. P. Daubert, S. McNitt, M. L. Andrews and A. D. Elkin. Long–term clinical course of patients after termination of ventricular tachyarrhythmia by an implanted defibrillator. *Circulation*, 110 (25): 3760–3765, 2004.

[56] S. Nattel, A. Maguy, S. Le Bouter and Y. H. Yeh. Arrhythmogenic ion-channel remodeling in the heart: heart failure, myocardial infarction, and atrial fibrillation. *Physiol. Rev.*, 87: 425–456, 2007.

[57] S. A. Niederer et al. Verification of cardiac tissue electrophysiology simulators using an N-version benchmark. *Philos. Trans. A Math. Phys. Eng. Sci.*, 369 (1954): 4331–4351, 2011.

[58] L. F. Pavarino and S. Scacchi. Multilevel additive Schwarz preconditioners for the Bidomain reaction-diffusion system. *SIAM J. Sci. Comput.*, 31: 420–443, 2008.

[59] J. M. B. Pinto and P. A. Boyden. Electrophysiologic remodeling in ischemia and infarction. *Cardiovasc. Res.*, 42: 284–297, 1999.

[60] J. Pu and P. Boyden. Alterations of Na currents in myocytes from epicardial border zone of the infarcted heart. A possible ionic mechanism for reduced excitability and postrepolarization refractoriness. *Circ. Res.*, 81: 110–119, 1997.

[61] B. B. Punske, Q. Ni, R. L. Lux, R. S. MacLeod, P. R. Ershler, T. J. Dustman, M. J. Allison and B. Taccardi. Spatial methods of epicardial activation time determination in normal hearts. *Ann. Biomed. Eng.*, 31: 781–792, 2003.

[62] T. Reichlin, M. Kuhne, C. Sticherling, S. Osswald and B. Schaer. Characterization and financial impact of implantable cardioverter-defibrillator patients without interventions 5 years after implantation. *QJM*, 104 (10): 849–857, 2011.

[63] D. E. Roberts, L. T. Hersh and A. M. Scher. Influence of cardiac fiber orientation on wavefront voltage, conduction velocity, and tissue resistivity in the dog. *Circ. Res.*, 44: 701–712, 1979.

[64] S. D. Roes, C. J. W. Borleffs, R. J. van der Geest, J. J. M. Westenberg, N. A. Marsan, T. A. M. Kaandorp, J. H. Reiber, K. Zeppenfeld, H. J. Lamb, A. de Roos, M. J. Schalij and J. J. Bax. Infarct tissue heterogeneity assessed with contrast-enhanced MRI predicts spontaneous ventricular arrhythmia in patients with ischemic cardiomyopathy and implantable cardioverter-defibrillator. *Circ. Cardiovasc. Imaging.*, 2 (3): 183-190, 2009.

[65] S. Rohr, J. P. Kucera and A. G. Kleber. Slow conduction in cardiac tissue. I. Effects of a reduction of excitability versus a reduction of electrical coupling on microconduction. *Circ. Res.*, 83: 781–794, 1998.

[66] S. L. Rutherford, M. L. Trew, G. B. Sands, I. J. LeGrice and B. H. Smaill. High-resolution 3-dimensional reconstruction of the infarct border zone. *Circ. Res.*, 111: 301–311, 2012.

[67] P. A. Scott, J. M. Morgan, N. Carroll, D. C. Murday, P. R. Roberts, C. R. Peebles, S. P. Harden and N. P. Curzen. The extent of left ventricular scar quantified by late gadolinium enhancement MRI is associated with spontaneous ventricular arrhythmias in patient with coronary artery disease and implantable cardioverter-defibrillators. *Circulation*, 4 (3): 324–330, 2011.

[68] R. M. Shaw and Y. Rudy. Ionic mechanisms of propagation in cardiac tissue. Roles of the sodium and L-type calcium currents during reduced excitability and decreased gap junction coupling. *Circ Res.*, 81 (5): 727–741, 1997.

[69] J. Sjoberg and M. Kanje. The initial period of peripheral nerve regeneration and the importance of the local environment for the conditioning lesion effect. *Brain. Res.*, 529 (1–2): 79–84, 1990.

[70] B. H. Smaill, J. Zhao and M. L. Trew. Three-dimensional impulse propagation in myocardium. Arrhythmogenic mechanisms at the tissue level. *Circ. Res.*, 112: 834–848, 2013.

[71] M. S. Spach and P. C. Dolber. Relating extracellular potentials and their derivatives to anisotropic propagation at a microscopic level in human cardiac muscle. Evidence for electrical uncoupling of side-to-side fiber connections with increasing age. *Circ. Res.*, 58 (3): 356–371, 1986.

[72] E. C. Stecker, C. Vickers, J. Waltz, C. Socoteanu, B. T. John, R. Mariani, J. H. McAnulty, K. Gunson, J. Jui and S. S. Chugh. Population–based analysis of sudden cardiac death with and without left ventricular systolic dysfunction: two-year findings from the Oregon Sudden Unexpected Death Study. *J. Am. Coll. Cardiol.*, 47 (6): 1161–1166, 2006.

[73] G. Tai, L. Fu, Y. Wang and Y. Zhang. Research progress on the association between connective tissue growth factor and ventricular remodeling after acute myocardial infarction. *Zhonghua Xin Xue Guan Bing Za Zhi*, 42 (5): 447–448, 2014.

[74] K. H. W. J. ten Tusscher, D. Noble, P. J. Noble and A. V. Panfilov. A model for human ventricular tissue. *Am. J. Phys. Heart Circ. Physiol.*, 286: H1573–H1589, 2004.

[75] K. H. W. J. ten Tusscher and A. V. Panfilov. Alternans and spiral breakup in a human ventricular tissue model. *Am. J. Phys. Heart Circ. Physiol.*, 291: H1088–H1100, 2006.

[76] N. A. Trayanova, P. M. Boyle, H. J. Arevalo and S. Zahid. Exploring susceptibility to atrial and ventricular arrhythmias resulting from remodeling of the passive electrical properties in the heart: a simulation approach. *Front. Physiol.*, 5: 435, 2014.

[77] L. Tung. *A bidomain model for describing ischemic myocardial D.C. potentials.* Ph.D. dissertation M.I.T., Cambridge, MA, 1978.

[78] P. C. Ursell, P. I. Gardner, A. Albala, J. J. Fenoglio Jr. and A. L. Wit. Structural and electrophysiological changes in the epicardial border zone of canine myocardial infarcts during infarct healing. *Circ. Res.*, 56: 436–451, 1985.

[79] M. Vaseghi, W. Zhou, J. Shi, O. A. Ajijola, J. Hadaya, K. Shivkumar and A. Mahajan. Sympathic innervation of the anterior left ventricular wall by right and left stellate ganglia. *Heart Rhythm*, 9 (8): 1303–1309, 2012.

[80] E. J. Vigmond, F. Aguel and N. A. Trayanova. Computational techniques for solving the bidomain equations in three dimensions. *IEEE Trans. Biomed. Eng.*, 49 (11): 1260–1269, 2002.

[81] E. J. Vigmond, F. Vadakkumpadan, V. Gurev, H. Arevalo, M. Deo, G. Plank and N. A. Trayanova. Towards predictive modelling of the electrophysiology of the heart. *Exp. Physiol.*, 94: 563–577, 2009.

[82] E. J. Vigmond, R. Weber dos Santos, A. J. Prassl, M. Deo and G. Plank. Solvers for the cardiac bidomain equations. *Prog. Biophys. Mol. Biol.*, 96 (1–3): 3–18, 2008.

[83] A. L. Wit and M. J. Janse. *The Ventricular Arrhythmias of Ischemia and Infarction: Electrophysiological Mechanisms.* Mount Kisco, NY: Futura Publishing Company, 1993.

[84] A. L. Wit, M. A. Allessie, F. I. Bonke, W. Lammers, J. Smeets and J. J. Fenoglio Jr. Electrophysiologic mapping to determine the mechanism of experimental ventricular tachycardia initiated by premature impulses. *Am. J. Cardiol.*, 49: 166–185, 1982.

[85] A. L. Wit, S. M. Dillon, J. Coromilas, A. S. Saltman and B. Waldecker. Anisotropy reentry in the epicardial border zone of myocardial infarcts. In J. Jalife (ed.), *Mathematical approaches to cardiac arrhythmias*, 86–108, Annals of the New York Academy of Sciences, vol. 591, 1990.

[86] A. T. Yan, A. J. Shayne, K. A. Brown, S. N. Gupta, C. W. Chan, T. M. Luu, M. F. Di Carli, H. G. Reynolds, W. G. Stevenson and R. Y. Kwong. Characterization of the peri-infarct zone by contrast-enhanced cardiac magnetic resonance imaging is a powerful predictor of post-myocardial infarction mortality. *Circulation*, 114 (1): 32–39, 2006.

[87] J-A. Yao, W. Hussain, P. Patel, N. S. Peters, P. A. Boyden and A. L. Wit. Remodeling of gap junctional channel function in epicardial border zone of healing canine infarcts. *Circulation*, 92: 437–443, 2003.

[88] S. Zaman, A. Narayan, A. Thiagalingam, G. Sivagangabalan, S. Thomas, D. L. Ross and P. Kovoor. Significance of repeat programmed ventricular stimulation at electrophysiology study for arrhythmia prediction after acute myocardial infarction. *Pacing Clin. Electrophysiol.*, 37 (7): 795–802, 2014.